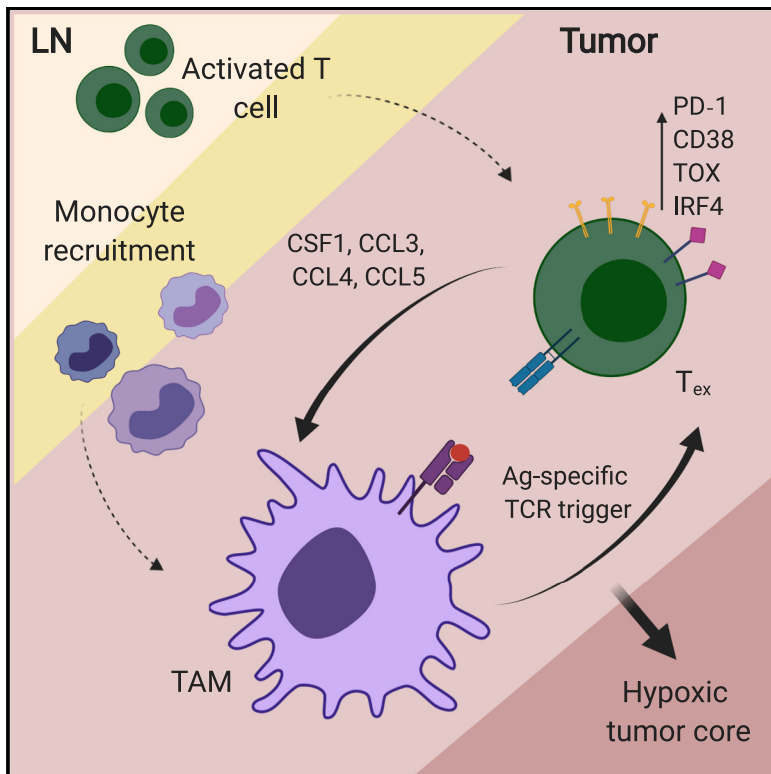


Spatiotemporal co-dependency between macrophages and exhausted CD8⁺ T cells in cancer

Graphical abstract



Authors

Kelly Kersten, Kenneth H. Hu,
Alexis J. Combes, ..., Julia Belk,
Ansuman T. Satpathy,
Matthew F. Krummel

Correspondence

matthew.krummel@ucsf.edu

In brief

Kersten et al. demonstrate a spatiotemporal co-dependency between tumor-associated macrophages (TAMs) and exhausted CD8⁺ T cells (T_{ex}) in cancer. T_{ex} shape myeloid cell recruitment and phenotype. Reciprocally, through antigen-specific stable synapses, TAMs contribute to exhaustion programs in CD8⁺ T cells, together with hypoxia, prominent in inner regions of the tumor.

Highlights

- Onset of T cell exhaustion in cancer is linked to TAM abundance
- T_{ex} express myeloid-related factors to shape myeloid cell recruitment and phenotype
- TAMs form uniquely long-lasting synapses with CD8⁺ T cells that license exhaustion
- ZipSeq reveals spatial coordination of TAM-T_{ex} axis in inner regions of tumors



Article

Spatiotemporal co-dependency between macrophages and exhausted CD8⁺ T cells in cancer

Kelly Kersten,^{1,2,8} Kenneth H. Hu,^{1,2,8} Alexis J. Combes,^{1,2,3} Bushra Samad,^{1,2,3} Tory Harwin,^{1,2} Arja Ray,^{1,2} Arjun Arkal Rao,^{1,2,3} En Cai,^{1,2} Kyle Marchuk,³ Jordan Artichoker,³ Tristan Courau,^{1,2,3} Quanming Shi,⁴ Julia Belk,⁵ Ansuman T. Satpathy,^{6,7,8} and Matthew F. Krummel^{1,2,3,8,9,*}

¹Department of Pathology, University of California, San Francisco, San Francisco, CA 94143, USA

²ImmunoX Initiative, University of California, San Francisco, San Francisco, CA 94143, USA

³UCSF CoLabs, University of California, San Francisco, San Francisco, CA 94143, USA

⁴Department of Personal Dynamic Regulomes, Stanford University School of Medicine, Stanford, CA 94305, USA

⁵Department of Computer Science, Stanford University, Stanford, CA 94305, USA

⁶Department of Pathology, Stanford University, Stanford, CA 94305, USA

⁷Gladstone–UCSF Institute of Genomic Immunology, San Francisco, CA 94158, USA

⁸Parker Institute for Cancer Immunotherapy, San Francisco, CA 94129, USA

⁹Lead contact

*Correspondence: matthew.krummel@ucsf.edu

<https://doi.org/10.1016/j.ccr.2022.05.004>

SUMMARY

T cell exhaustion is a major impediment to antitumor immunity. However, it remains elusive how other immune cells in the tumor microenvironment (TME) contribute to this dysfunctional state. Here, we show that the biology of tumor-associated macrophages (TAMs) and exhausted T cells (T_{ex}) in the TME is extensively linked. We demonstrate that *in vivo* depletion of TAMs reduces exhaustion programs in tumor-infiltrating CD8⁺ T cells and reinvigorates their effector potential. Reciprocally, transcriptional and epigenetic profiling reveals that T_{ex} express factors that actively recruit monocytes to the TME and shape their differentiation. Using lattice light sheet microscopy, we show that TAM and CD8⁺ T cells engage in unique, long-lasting, antigen-specific synaptic interactions that fail to activate T cells but prime them for exhaustion, which is then accelerated in hypoxic conditions. Spatially resolved sequencing supports a spatiotemporal self-enforcing positive feedback circuit that is aligned to protect rather than destroy a tumor.

INTRODUCTION

Cancer immunotherapy—harnessing the patient’s immune system to fight cancer—has revolutionized cancer treatment strategies. However, a large proportion of patients does not show clinical response, and the mechanisms underlying resistance are still poorly understood. CD8⁺ T cells are critical mediators of antitumor immune responses and are the main target for current immunotherapy approaches. Tumor infiltration of CD8⁺ T cells correlates with improved prognosis and beneficial responses to immune checkpoint blockade as compared to non-infiltrated tumors (Galon et al., 2006; Tumeh et al., 2014). However, those CD8⁺ T cells are frequently non-functional due to their exhausted state, characterized by the expression of inhibitory molecules, including PD-1, CD38, and TOX, and the loss of cytotoxic effector function (Wherry et al., 2007; Doering et al., 2012; Schietinger et al., 2016; Pauken et al., 2016; Scott et al., 2019; Khan et al., 2019). Several studies have shown that chronic antigen exposure and stimulation of the T cell receptor (TCR) are required for exhaustion programs in T cells (Utzschneider et al., 2016; Scott et al., 2019; Oliveira et al., 2021). However, how this is orchestrated in the tumor microenvironment (TME) is unclear.

The immune composition of the TME plays an important role in regulating effective antitumor T cell responses (Binnewies et al., 2018). Across solid tumors, the majority of immune cells in the TME frequently comprise antigen-presenting myeloid cells (APCs), and of these, tumor-associated macrophages (TAMs) are typically the most abundant (DeNardo et al., 2011; Ruffell et al., 2012; Broz et al., 2014). TAM abundance is correlated with poor prognosis in a variety of solid tumor types (Zhang et al., 2012; Gentles et al., 2015), and many studies report on their immunosuppressive role in cancer progression and dissemination (DeNardo and Ruffell, 2019). Conversely, some studies report immunostimulatory and antitumor functions through the expression of tumor necrosis factor (TNF) and inducible nitric oxide synthase (iNOS), or upon treatment with CD40 agonists (Beatty et al., 2011; Klug et al., 2013). Similar to a rare population of conventional dendritic cells (cDC1), which have been described to be potent activators of antitumor T cells (Broz et al., 2014; Roberts et al., 2016; Salmon et al., 2016; Spranger et al., 2017), TAMs have the potential to phagocytose large amounts of tumor-associated antigens, but fail to successfully support T cell activation (Engelhardt et al., 2012; Broz et al., 2014). Interestingly, intravital imaging studies have shown that



antigen-specific CD8⁺ T cells preferentially localize in TAM-rich areas in the TME, and form tight interactions that persist over time (Boissonnas et al., 2013; Broz et al., 2014; Peranzoni et al., 2018).

Here, we dissect the molecular mechanisms of immune co-differentiation, by which TAMs and exhausted CD8⁺ T cells (T_{ex}) sustain each other's maturation and presence in the TME through long-lived antigen-specific synaptic contacts. Our study reveals a mechanistic link through an antigen-driven positive feedback loop and offers a possible path whereby T cells and TAMs may equally contribute to initial and sustained tumor immune evasion.

RESULTS

CD8⁺ T cell exhaustion correlates with macrophage abundance in the TME

To study how myeloid immune cells contribute to CD8⁺ T cell exhaustion in the TME, we focused on the concurrent events during the onset of exhaustion programs in tumor-infiltrating CD8⁺ T cells in mouse models of melanoma (B78ChOVA and B16ChOVA) and spontaneous breast cancer (MMTV-PyMTCh-OVA) (Figure S1A). At different time points during tumor growth, we adoptively transferred ovalbumin (OVA)-specific OT-I CD8⁺ T cells into tumor-bearing mice, focusing on (1) early-arrival T cells that were recently recruited to the TME (T_{ex} day [d] 4) and (2) T cells that have resided in the TME for 14 days and have demonstrably upregulated PD-1, CD38, TOX, and CD5 as assessed by flow cytometry (T_{ex} d14) (Figure S1B). Both of these populations demonstrated reduced production of the cytokines interferon- γ (IFN- γ) and TNF- α when compared to activated CD44⁺ endogenous CD8⁺ T cells in the tumor-draining lymph node (TdLN) (Figures S1C and S1D). The onset of exhaustion and dysfunction in CD8⁺ T cells upon tumor infiltration was antigen specific, because irrelevant lymphocytic choriomeningitis virus (LCMV)-specific P14 CD8⁺ T cells did not acquire phenotypic markers of exhaustion when compared to OT-I CD8⁺ T cells (Figures S1E–S1H). However, the ability to produce effector cytokines IFN- γ and TNF- α was blunted equivalently in endogenous, P14, and OT-I CD8⁺ T cells upon tumor residence (Figures S1I and S1J). The loss of those markers may represent a natural decay process post-activation or universal non-antigen-specific suppression mechanisms (e.g., immunosuppressive cytokines such as interleukin-10 [IL-10], transforming growth factor β [TGF- β], and iNOS) in the TME.

TAMs comprised the majority of myeloid cells in B78ChOVA melanomas, in line with previous studies (Broz et al., 2014; Gentles et al., 2015; Cheng et al., 2021), and their abundance increased during tumor progression, while the fraction of CD103⁺ cDC1 and CD11b⁺ cDC2 diminished (Figure S1K). Recognizing the stoichiometric abundance of TAMs as possible APCs, we sought to study the role of TAMs in the onset of CD8⁺ T cell exhaustion by subjecting tumor-bearing mice to antibody-mediated blockade of colony-stimulating factor 1-colony stimulating factor 1 receptor (CSF1-CSF1R) signaling (Figures 1A, S1O, and S1R). Blockade of CSF1-CSF1R induced a significant reduction in the proportion of CD11b⁺F4/80⁺ TAMs in tumors (Figures 1B, 1C, S1L, S1P, and S1S) and a modest increase in neutrophils (Figure S1L). Of note, CSF1R blockade did not affect the phenotype of

TAM as determined by flow cytometric analysis of the positive fraction (Figure S1M) and expression levels of a variety of phenotypic markers on TAMs (Figure S1N).

Interestingly, without affecting the proportion of infiltrating T cells (Figure S1L), acute TAM-depletion resulted in a concurrent reduction in the expression of exhaustion markers PD-1, CD38, and TOX on tumor-infiltrating CD44⁺ OT-I CD8⁺ T cells (Figures 1D, S1Q, and S1T). Moreover, the resultant CD44⁺ OT-I CD8⁺ T cells produced higher levels of IFN- γ and TNF- α in anti-CSF1R compared to isotype-treated mice (Figures 1E and 1F), but they only modestly affected tumor size (Figure S1U). We found that the expression of PD-1, CD38, and TOX on tumor-infiltrating CD44⁺ OT-I CD8⁺ T cells positively correlates with the abundance of TAMs in the TME, measured across 25 mice in 3 independent experiments subjected to anti-CSF1R or isotype treatment (Figure 1G). In line with this, flow cytometric profiling of CD8⁺ tumor-infiltrating lymphocytes (TILs) in a cohort of 20 patients with renal cell carcinomas, which are rich in myeloid and T cells (Combes et al., 2022; Mujal et al., 2022), demonstrated a strong association between PD-1 and CD38 (but not CTLA-4) expression and the degree to which the myeloid cells of a patient had differentiated toward macrophages as compared to monocytes in the TME (Figure 1H). We used this ratio as the pure number of macrophages did not show this association (data not shown).

CD8⁺ T_{ex} express monocyte/macrophage-related factors upon prolonged residence in the TME

To test whether there is a mechanistic link between TAM abundance and CD8⁺ T cell exhaustion, we isolated early (T_{ex} d4) and late (T_{ex} d14) exhausted OT-I CD8⁺ T cells from B78ChOVA tumors and compared their transcriptional profile to that of splenic naive CD44⁻ OT-I CD8⁺ T cells by RNA sequencing (RNA-seq). As expected, T_{ex} d14 showed an enhanced expression of known markers associated with exhaustion (Sade-Feldman et al., 2018), including but not limited to *Cd44*, *Pdcdf1*, *Cd38*, *Irf4*, *Havcr2*, and *Lag3*, while the expression of naive precursor genes *Sell*, *Tcf7*, and *Il7r* was enriched in T_{naive} cells (Figure 2A). Interestingly, pathway enrichment analysis of genes with a fold enrichment >5 in T_{ex} revealed the dramatic enrichment of pathways involved in “abnormal cytokine secretion and “impaired macrophage chemotaxis” (Figure 2B). A closer analysis of individual genes demonstrated that the expression of genes associated with naive precursor T cell states decreased and genes previously associated with exhaustion increased in T_{ex} d14 versus T_{ex} d4 (Figure 2C), consistent with previous reports (Pauken et al., 2016; Schietinger et al., 2016; Sade-Feldman et al., 2018). Interestingly, a large set of myeloid-related genes was highly upregulated in CD8⁺ T_{ex} , and most of these increased with prolonged residence in the TME (Figures 2C and S2A). Interestingly, the majority of the myeloid-related genes upregulated in CD8⁺ T_{ex} are known regulators of monocyte/macrophage biology, while the expression of *Flt3L*, a formative cytokine for CD103⁺ cDC1 (Barry et al., 2018), was downregulated in T_{ex} (Figure 2C). The increased expression of several of these myeloid-related genes was confirmed on independent sample sets transcriptionally by qRT-PCR (Figure S2B) and by the quantification of secreted protein (Figure S2C). Of note, the majority of these changes was not observed in effector CD8⁺

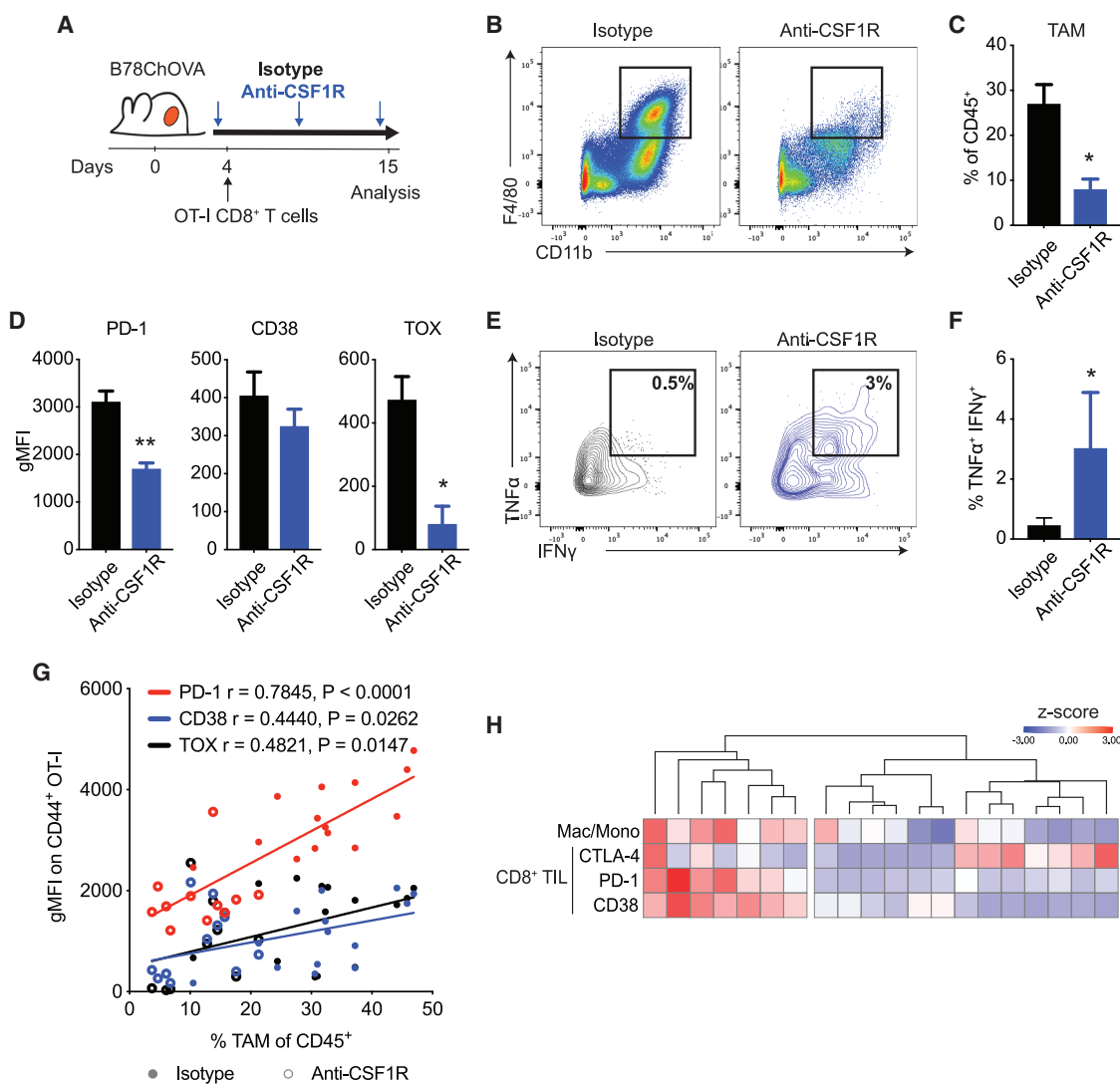


Figure 1. CD8⁺ T cell exhaustion correlates with macrophage abundance in the TME

(A) Experimental setup. Weekly anti-CSF1R or isotype antibody treatment was initiated 1–2 days after B78ChOVA tumor inoculation. OVA-specific OT-I CD8⁺ T cells were adoptively transferred 2–3 days after tumor inoculation. Mice were sacrificed at day 15 and the tumors were harvested for analysis.

(B and C) Representative flow plots (B) and quantification (C) of CD11b⁺ F4/80⁺ macrophages in isotype and anti-CSF1R-treated tumors. n = 5 mice/group.

(D) Surface (PD-1 and CD38) and intracellular (TOX) expression on intratumoral CD44⁺ OT-I CD8⁺ T cells from isotype and anti-CSF1R-treated mice. n = 5 mice/group.

(E and F) Representative contour plots (E) and quantification (F) of IFN- γ ⁺TNF- α ⁺ polyfunctional CD44⁺ OT-I CD8⁺ T cells in tumors of isotype and anti-CSF1R-treated mice. n = 8–9 mice/group. Pooled data from 2 independent experiments.

(G) Spearman correlation between geometric mean fluorescence intensity (gMFI) of PD-1, CD38, and TOX expression on CD44⁺ OT-I CD8⁺ T cells and percentage of TAM of CD45⁺ cells in tumors treated with isotype (solid) or anti-CSF1R antibody (open). n = 11–14 mice/group.

(H) Heatmap showing clustering of normalized Z scores of CTLA-4, PD-1, and CD38 expression on CD8⁺ TILs and macrophage:monocyte ratio in 20 fresh human kidney renal cell carcinoma samples (rows) determined by flow cytometry. All of the data are means \pm SEMs; *p < 0.05, **p < 0.01, as determined by the Mann-Whitney U test.

See also Figure S1.

T cells (T_{eff}), suggesting a unique exhaustion-related expression profile in CD8⁺ T cells that is acquired upon prolonged residence in the TME. Increased expression of these myeloid-related genes was detected in both endogenous and OT-I T_{ex} cells, and thus seems independent of antigen reactivity.

Epigenetic profiling using assay for transposase-accessible chromatin with sequencing (ATAC-seq) confirmed a significant enhancement of overall chromatin accessibility near the transcript

tion start site of the genes encoding these myeloid-related genes in T_{ex} d14 versus T_{naive} cells (Figure 2D). A more detailed analysis of the signal tracks of chromatin accessibility peaks at different gene loci revealed that *Tox*, a major transcriptional and epigenetic regulator of T cell exhaustion (Alfei et al., 2019; Khan et al., 2019; Scott et al., 2019; Yao et al., 2019), as well as other well-known genes associated with exhaustion programs (*Pdcd1*, *Cd38*, *Havcr2*, *Ctla4*, *Lag3*, and *Entpd1* (Pauken et al., 2016; Philip

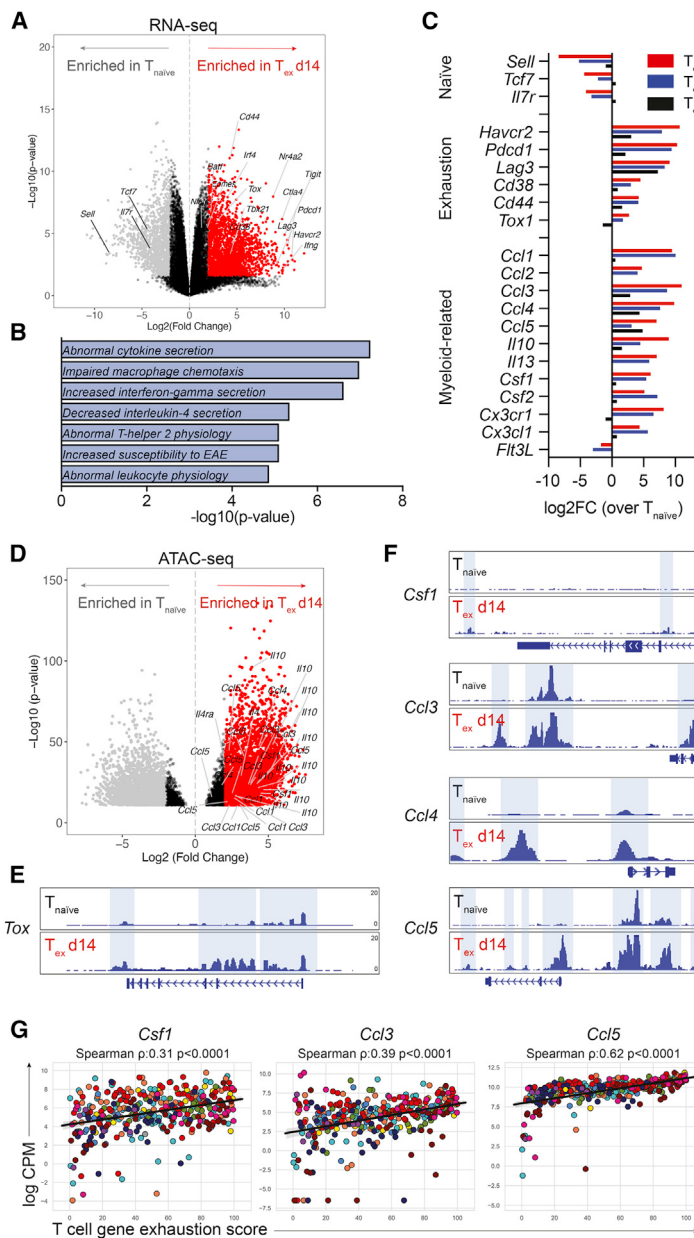


Figure 2. Exhausted CD8⁺ T cells (T_{ex}) express myeloid-related factors

(A) Volcano plot showing differential gene expression in tumor-infiltrating CD44⁺ OT-I CD8⁺ T_{ex} d14 cells (red) compared to splenic CD44⁻ OT-I CD8⁺ T_{naive} cells (gray) by RNA-seq. Colored dots (gray and red) represent genes with a log2FC > 2 and false discovery rate (FDR) < 0.05.

(B) Gene set enrichment analysis of differentially expressed genes (DEGs) ($\log_{2}\text{FC} > 5$ and $p < 0.05$) enriched in T_{ex} d14 versus T_{naive} using the MGI Mammalian Phenotype Level 4 library.

(C) Average gene expression in T_{eff} (black), $T_{\text{ex}} \text{ d4}$ (blue), and $T_{\text{ex}} \text{ d14}$ (red) normalized to T_{naive} as determined by RNA-seq.

(D) Volcano plot showing differential chromatin accessibility at transcriptional start sites in loci of myeloid genes in tumor-infiltrating CD44⁺ OT-I CD8⁺ T_{ex} d14 cells compared to splenic CD44⁻ OT-I CD8⁺ T_{naive} cells by ATAC-seq. Colored dots (gray and red) represent genes with a log2FC > 2 and FDR < 0.05.

(E) and (F) ATAC-seq signal tracks at the *Tox* (E), *Csf1*, *Ccl3*, *Ccl4*, and *Ccl5* (F) loci highlighting differential chromatin accessibility peaks in CD44⁺ OT-I CD8⁺ T_{ex} cells (d14) compared to splenic CD44⁻ OT-I CD8⁺ T_{naive} cells.

(G) Correlation of normalized expression of *Csf1*, *Ccl3*, and *Ccl5* transcripts and exhaustion score in fluorescence-activated cells sorting (FACS) sorted human intratumoral T cells across multiple human cancer indications.

See also Figure S2.

et al., 2017), showed increased chromatin accessibility at promoter regions in T_{ex} when compared to T_{naive} (Figures 2E and S2D). This enhanced accessibility was also observed for myeloid-related genes *Csf1*, *Ccl3*, *Ccl4*, and *Ccl5* in T_{ex} when compared to T_{naive} (Figure 2F). In addition, using transcriptional profiles of T cells isolated from human cancers, we found that increased expression of a T cell exhaustion score correlated significantly with the expression of *Csf1*, *Ccl3*, and *Ccl5* in T cells in a dataset comprising hundreds of patients across a dozen cancer indications (Combes et al., 2022) (Figure 2G).

CD8⁺ T_{ex} shape the myeloid compartment in mouse melanoma

To directly study the functional significance of chemokine gene expression by T_{ex} , we adopted a transwell experimental system

using OT-I T cells with varying activation states in the bottom well, and bone marrow-derived monocytes in the upper transwell insert (Figure 3A). After 24 h of culture, significantly more monocytes had migrated through the transwell membrane toward T_{ex} when compared to T_{eff} , T_{naive} , or no T cells (Figure 3B), demonstrating that T_{ex} actively secrete factors that recruit monocytes, while T cells in other activation states do not. Phenotypic analysis by flow cytometry revealed that

monocytes co-cultured for 2 days with T_{ex} also show increased uniformity and/or magnitude of expression of CD80, CD86, H2Kb, and major histocompatibility complex class II (MHC-II) when compared to T_{eff} , T_{naive} , or no T cells (Figure 3C), suggesting that T_{ex} -derived factors augment antigen-presentation potential in differentiating myeloid cells.

To assess whether T_{ex} actively shape the myeloid compartment in tumors *in vivo*, we were faced with a dearth of available models that allow for specific (conditional) deletion of exhausted T cells from the TME. Therefore, we decided to use a more widely used approach to systemically deplete CD4⁺ or CD8⁺ T cells from B7-1ChOVA-bearing mice using depleting antibodies (Figure 3D). Interestingly, while the ratio of monocytes to macrophages did not change upon CD4⁺ or CD8⁺ T cell depletion (Figure 3E), their phenotype was drastically affected by CD8⁺

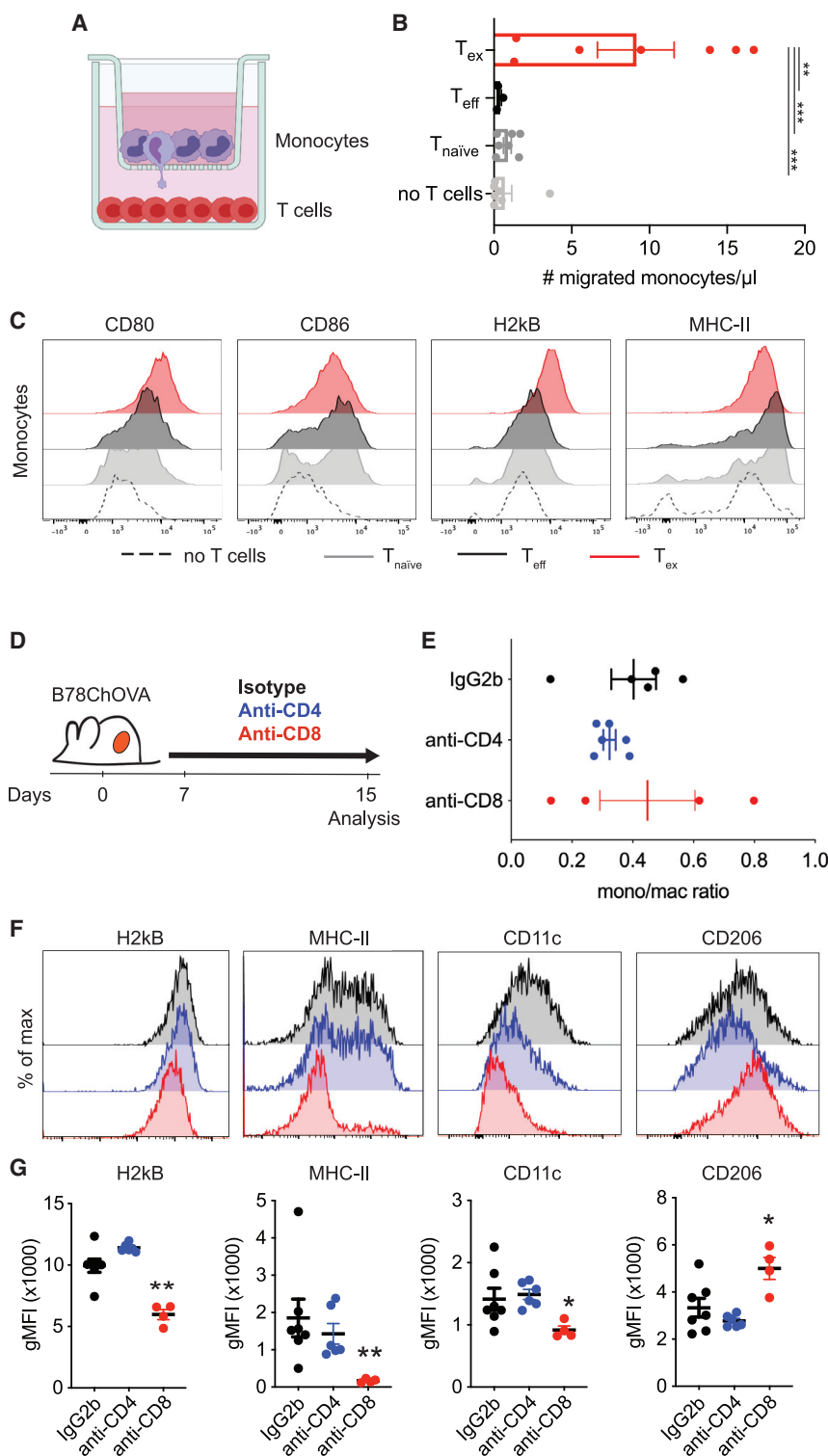


Figure 3. CD8⁺ T_{ex} recruit monocytes to the TME and shape macrophage phenotype

(A) Experimental setup of *in vitro* recruitment assay. Bone marrow-derived monocytes are cultured on transwell inserts (5 µm pore size) and T cells (OT-I T_{naive} , T_{eff} , and T_{ex}) are plated in the bottom well.

(B) Quantification of recruited monocytes after 24 h. Data combined from 2 independent experiments. Statistical significance was determined by 1-way ANOVA with Holm-Sidak's multiple testing correction.

(C) Representative histograms of expression of surface markers on monocytes after 48 h of co-culture with T_{naive} , T_{eff} , and T_{ex} cells.

(D) Experimental setup of *in vivo* CD4⁺ and CD8⁺ T cell depletion in B78ChOVA-bearing mice. Treatment with anti-CD4/CD8 antibodies or isotype was initiated 7 days after tumor inoculation and continued until mice were sacrificed.

(E and F) Monocyte:macrophage ratio of the proportion of Ly6C^{hi} monocytes and F4/80⁺ macrophages (gated on CD45⁺ cells) in the B78ChOVA TME after isotype, anti-CD4, and anti-CD8 treatment. n = 4–7 mice/group.

(F and G) Representative histograms (F) and quantification (G) of H2kb, MHC-II, CD11c, and CD206 expression on CD11b^{hi}F4/80⁺ macrophages in B78ChOVA tumors after isotype, anti-CD4, and anti-CD8 treatment. Statistical significance was determined using the Mann-Whitney U test. All of the data are means \pm SEMs; *p < 0.05, **p < 0.01, ***p < 0.001.

See also Figure S3.

3G), suggesting that CD8⁺ T cells specifically shape the myeloid cell phenotype in the TME favoring an “M1-like” antigen-presenting state.

To test whether the production of CSF1 by lymphocytes had any functional relevance for myeloid composition in the TME, we generated mixed bone marrow chimeras in which *Rag1*^{−/−} bone marrow was mixed 50:50 with either *Csf1*^{op/op} or *Csf1*^{op/+} bone marrow and transferred into lethally irradiated *Rag1*^{−/−} recipient mice (Figure S3A). After a recovery period of 6–10 weeks, these mice were inoculated with B78ChOVA melanomas for 21 days, after which the myeloid compartment in the TME was analyzed by flow cytometry. CSF1 deficiency in lymphocytes (*Rag1*^{−/−}:*Csf1*^{op/op} chimeras) did not affect primary tumor

growth (Figure S3B) and modestly reduced the influx of total CD45⁺ leukocytes compared to control animals (*Rag1*^{−/−}:*Csf1*^{op/+}) (Figure S3C). In the myeloid compartment, the proportion of Ly6C⁺ monocytes was significantly enriched in *Rag1*^{−/−}:*Csf1*^{op/op} chimeras, while macrophage proportions were lower, resulting in an increased monocyte/macrophage ratio in

T cell depletion in ways that are consistent with the results of our *in vitro* co-cultures. CD11b^{hi}F4/80⁺ TAMs showed significantly reduced expression of H2kb, MHC-II, and CD11c in the absence of CD8⁺ T cells, but not CD4⁺ T cells (Figures 3F and 3G). In addition, CD8⁺ T cell depletion resulted in increased expression of “pro-tumorigenic M2 marker” CD206 on TAMs (Figures 3F and

Rag1^{-/-}:Csf1^{op/op} chimeras (Figure S3D). The proportion of CD103⁺ cDC1 and CD11b⁺ cDC2 were not appreciably modulated by CSF1 deficiency in lymphocytes (Figure S3E). In line with the results presented in Figures 3F and 3G, the levels of H2kB, MHC-II, and CD11c on CD11b⁺F4/80⁺ TAMs were lower in *Rag1^{-/-}:Csf1^{op/op}* chimeras when compared to *Rag1^{-/-}:Csf1^{op/+}* chimeras (Figure S3F), while the expression of CD86 and CD206 was modestly increased. Despite the large biological variation among these samples, the results support the notion that CD8⁺ T_{ex}, at least partially through the expression of CSF1, contribute to TAM maturation and induce an antigen-presentation phenotype in the TME.

Macrophages and CD8⁺ T cells engage in unique long-lived interactions and synapse formation

Since our data suggest that CD8⁺ T_{ex} shape the myeloid cell phenotype toward an antigen-presenting state, we took a more detailed look at the interactions between TAM and CD8⁺ T cells in the TME. Using 2-photon microscopy, we have previously shown that newly infiltrated antigen-specific CD8⁺ T cells in the TME preferentially localize in TAM-rich areas and are captured in prolonged interactions with TAM that result in the onset of exhaustion programs (Engelhardt et al., 2012; Broz et al., 2014; Boldajipour et al., 2016). In line with these results, ex vivo coupling assays using single-cell suspensions (enriched for CD45⁺ cells) from B16F10 and B16ChOVA tumors confirmed that OT-I CD8⁺ T cells preferentially form doublets with myeloid cells, and specifically TAM, in an antigen-dependent manner (Figures S4A–S4C). Moreover, after the adoptive transfer of both OT-I and P14 CD8⁺ T cells in B78ChOVA-bearing mice, we found that (after enzymatic digestion) both the proportion of total T cell doublets and the proportion of those that are coupled to a TAM are significantly higher among OT-I versus P14 or endogenous CD8⁺ T cells (Figure S4D), suggesting the preferential formation of antigen-specific TAM-T cell doublets. Conventional wide field imaging demonstrated that outside of the context of the TME, previously activated OT-I CD8⁺ T cells interact significantly longer with TAMs sorted from OVA-expressing tumors as compared to *in vitro*-generated bone marrow-derived dendritic cells (BMDCs) unloaded or loaded with the cognate peptide SIINFEKL (SL8) (Figures 4A and 4B), demonstrating a persistent interaction between TAM and CD8⁺ T cells, despite their consistent inability to stimulate T cell proliferation.

Using lattice light sheet microscopy, we found that this stable interaction between TAMs and CD8⁺ T cells results in small-scale clustering of TCRs at the TAM interaction site on CD8⁺ T cells (Figures 4C–4E and S4E; Video S1), consistent with this being a signaling interaction. Calcium imaging revealed that, unlike CD103⁺ cDC1—potent inducers of CD8⁺ T cell activation (Broz et al., 2014; Roberts et al., 2016; Salmon et al., 2016; Spranger et al., 2017)—which trigger a transient flux, B16ChOVA-derived TAMs induce a weak but long-lasting Ca²⁺ flux in CD8⁺ T cells upon recognition of a cognate antigen (Figure 4F, left). This flux was likely antigen dependent since TAMs and CD103⁺ cDC1 isolated from B16F10 melanomas did not induce a TCR trigger in OT-I CD8⁺ T cells (Figure 4F, right). While the transient Ca²⁺ flux triggered by CD103⁺ cDC1 is sufficient to induce the proliferation of CD8⁺ T cells, the antigen-specific

trigger provided by TAM fails to support proliferation (Figure 4G). Thus, despite actively and profoundly engaging T cells in a unique long-lasting antigen-specific synaptic interaction, TAMs fail to fully support CD8⁺ T cell activation and proliferation.

Unique TCR engagement by TAMs induces exhaustion programs in CD8⁺ T cells

To take a more detailed look at the TAM-induced “dysfunctional” TCR trigger, we examined *ex vivo* co-cultures of previously activated OT-I CD8⁺ T cells with TAMs or CD103⁺ cDC1 isolated from B16ChOVA and B16F10 melanomas, or *in vitro*-generated BMDC devoid of antigen as a negative control. As expected, after 3 days of co-culture, only CD8⁺ T cells that had encountered CD103⁺ cDC1 expressing their cognate antigen displayed a high level of CD44 (CD44^{hi}) high level of interferon regulatory factor 4 (IRF4^{hi}) fully activated phenotype (Figure 5A). Interestingly, when compared to the successful signal provided by CD103⁺ cDC1, TAMs only modestly induced the expression of activation marker CD44, while providing a similar strength in TCR trigger as suggested by the level of IRF4 expression (Figure 5A). In chronic viral infections, IRF4 has been implicated as a main regulator of transcriptional circuits inducing and sustaining T cell exhaustion (Man et al., 2017). In line with this notion, TAMs induced a significant increase in the expression of PD-1 and TOX in CD8⁺ T cells in an antigen-specific manner and similar to CD103⁺ cDC1 (Figure 5A), but nevertheless fail to support proliferation (Figure 4G). The addition of exogenous SL8 peptide to TAM was unable to rescue CD8⁺ T cell activation and proliferation (Figure S5A). Moreover, the TAM-induced exhaustion phenotype failed to produce effector cytokines IFN-γ and TNF-α (Figure S5B), suggesting that these cells are indeed dysfunctional.

Previous work has shown that hypoxia, in combination with chronic antigenic stimulation but not in the absence of stimulation, is required to obtain a “full blown” exhausted phenotype in CD8⁺ T cells *in vitro* (Scharping et al., 2021). To study whether the signals from TAM-T_{ex} interactions are sufficient to “prime” T cells for exhaustion despite being deficient at inducing their proliferation, we performed co-culture experiments under hypoxic (1.5% O₂) and normoxic (21% O₂) conditions. Interestingly, the proportion of PD-1⁺ CD8⁺ T cells induced by B16ChOVA-derived TAMs was much more pronounced when cultured in hypoxic conditions as compared to normoxia, especially when TAMs were numerically in excess (Figures 5B and 5C). Together, these data demonstrate that TAMs can prime the onset of exhaustion programs in CD8⁺ T cells, a process that is exacerbated in hypoxic conditions.

Using the hypoxia tracer pimonidazole, we found that B78ChOVA melanomas show highly hypoxic areas toward the inner regions of the tumor, and away from CD31⁺ blood vessels (Figure 5D). Moreover, we find that these hypoxic regions are surrounded by patches of CD11b⁺ macrophages (Figure 5D). In line with this observation, the expression of hypoxia-related genes (*Car9*, *Hif1a*, *Hif2a*, *Glut1*, *Vegfa*, *Vhl*) was upregulated in exhausted CD8⁺ T cells upon prolonged residence in the TME (Figure 5E), suggesting that tumor-infiltrated T_{ex} experience severe hypoxia in the TME. Interestingly, flow cytometric analysis revealed that TAM experience more severe levels of hypoxia compared to exhausted CD8⁺ T cells and CD45[−] tumor cells

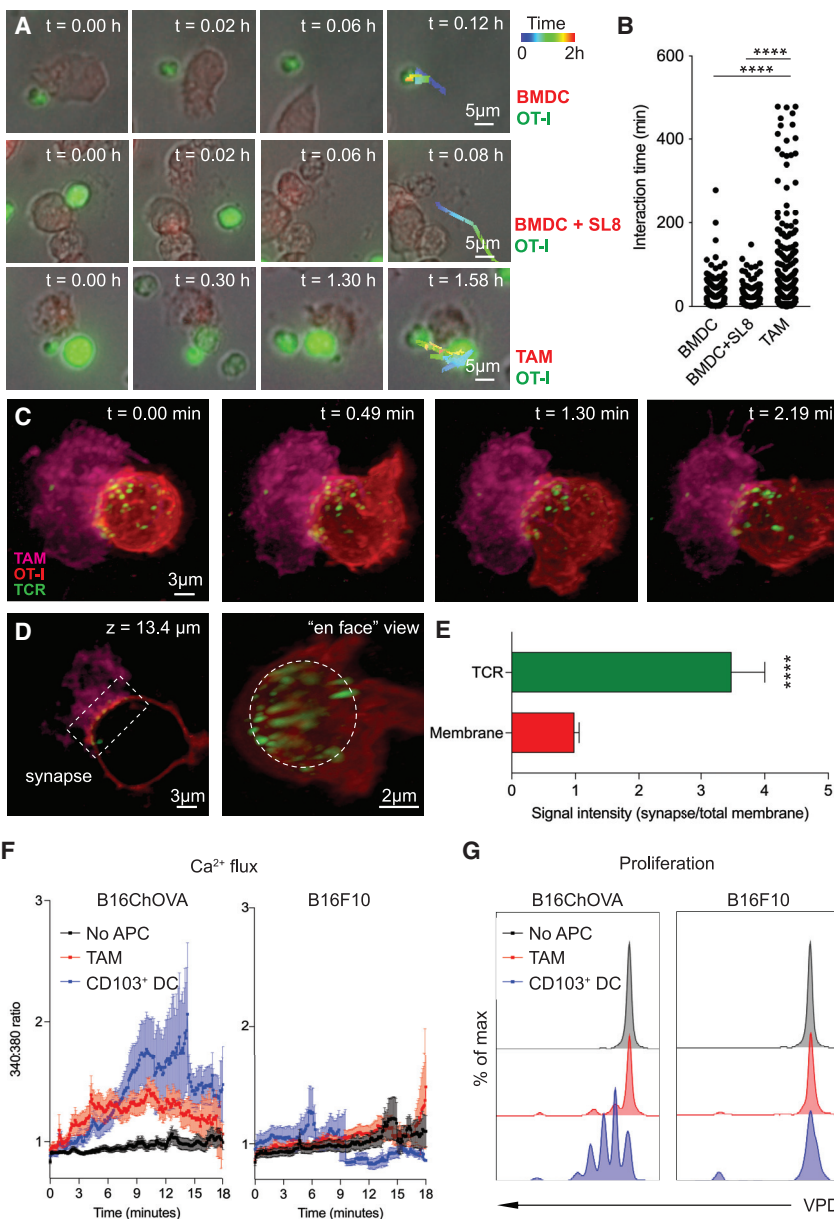


Figure 4. TAMs uniquely engage CD8⁺ T cells in antigen-specific long-lived synaptic interactions

(A) Representative images of *ex vivo* interactions between mTomato⁺ APC (BMDC, BMDC + SL8, or B78ChOVA-derived TAMs) and carboxy-fluorescein succinimidyl ester (CFSE)-labeled previously activated CD8⁺ OT-I T cells over time using conventional wide field microscopy. Scale bar, 5 μm.

(B) Quantification of interaction time. n = 3,452 TAMs, n = 6,134 BMDCs, n = 3,320 BMDCs + SL8. Statistical significance was determined using the 1-way ANOVA test with Holm-Sidak's multiple comparison correction.

(C) Representative images of the interaction between mTomato⁺ TAMs sorted from B78ChOVA melanomas (magenta) and previously activated CD8⁺ OT-I T cells labeled with CD45-AF647 (red), with the H57 TCRβ labeled with AF488 by lattice light sheet imaging. Scale bar, 3 μm.

(D) Z slice (left) and *en face* view (right) of the TAM-CD8⁺ T cell interaction site showing TCR clustering in the immunological synapse (box [left] and dotted circle [right]).

(E) Quantification of polarized TCR clustering by determining the ratio of signal intensity of the red (membrane) or green channel (TCR) at the synapse site normalized to the entire membrane. n = 12 T cells. Statistical significance was determined using the Mann-Whitney U test.

(F and G) Quantification of immediate Ca²⁺ flux by FURA-2AM imaging (F) and proliferation after 72 h by dilution of violet proliferation dye (VPD) (G) in previously activated CD8⁺ OT-I T cells after interaction with TAMs or CD103⁺ DCs isolated from B16ChOVA or B16F10 tumors. Negative control represents CD8⁺ OT-I T cells that did not touch an APC (no APC). All of the data are means ± SEMs; *p < 0.05, **p < 0.01, ***p < 0.001, ****p < 0.0001.

See also Video S1 and Figure S4.

myeloid cells in B78ChOVA melanomas (data not shown). We used this model to define distinct regions in the tumor such as the outer rim and middle and inner compartments based on the mCherry signal in

cancer cells and the Venus expression in CD206⁺ myeloid cells (Figure 6A) and apply unique Zipcodes to the surface of immune cells in each of those regions. After the dissociation of tumors, we sorted CD45⁺ immune cells and encapsulated them for our modified 10x Genomics single-cell RNA-seq (scRNA-seq) workflow (Hu et al., 2020).

Uniform manifold approximation and projection (UMAP) analysis of the entire immune compartment revealed prototypical and predominant clusters of T cells and monocytes/macrophages, as well as smaller clusters of natural killer (NK) cells and DCs (Figures 6B, S6B, and S6C). Some of these populations were enriched in specific regions in the TME (Figure 6C). We further subsampled the CD8⁺ T cell subset and revealed that CD8⁺ T cells with a more naive phenotype are enriched at the outer regions of the tumor, while CD8⁺ T_{ex} mainly localize deeper

(Figures 5F and 5G). Moreover, the degree of hypoxia was dramatically reduced in residual TAMs, but not in T_{ex}, after CSF1R blockade (Figures 5F and 5G).

ZipSeq mapping reveals spatial coordination of TAM-T_{ex} interaction dynamics in the TME

To better understand the spatial coordination of the dynamic interplay between TAM and T_{ex} in the TME, we used ZipSeq, a spatial transcriptomics approach that allows us to map gene expression patterns in single cells based on their localization in the TME by printing barcodes directly onto cells in tissue (Hu et al., 2020). We used a Cd206-LSL-Venus-DTR mouse model in which the expression of a Venus fluorescent reporter is driven by the endogenous Cd206 promoter (Figure S6A). When crossed to the Csf1r^{Cre} strain, we found Venus labeling of the majority of tumor-associated

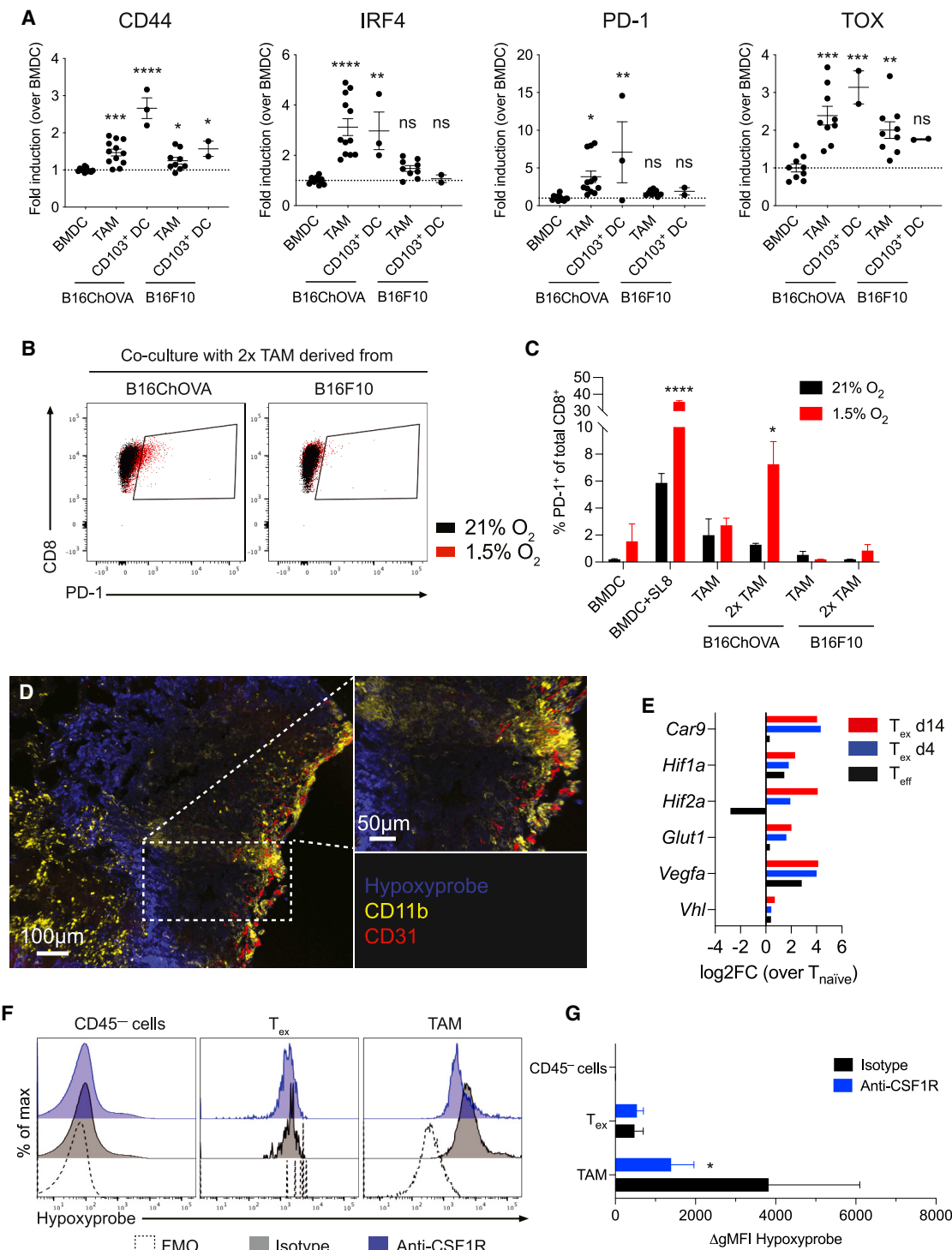


Figure 5. TAM engagement contributes to induction of exhaustion programs in CD8⁺ T cells in an antigen-specific manner

(A) Flow cytometric analysis of CD44, IRF4, PD-1, and TOX expression in previously activated CD8⁺ OT-I T cells co-cultured for 72 h with *in vitro*-generated BMDCs and TAMs or CD103⁺ DCs isolated from B16ChOVA or B16F10 tumors. Data are presented as fold induction over BMDC. Cumulative data from 4 independent experiments. All of the data are plotted as means ± SEMs. One-way ANOVA with Holm-Sidak correction for multiple comparisons.

(B and C) Representative dot plots (B) and quantification (C) of PD-1⁺ expression on previously activated CD8⁺ OT-I T cells after co-culture with *in vitro*-generated BMDCs ± SL8, and TAMs isolated from B16ChOVA or B16F10 tumors. Ratio of APC:T cell was 1:4 or 1:2 (2 × TAM). Plates were incubated in normoxic (21% O₂) and hypoxic (1.5% O₂) conditions for 3 days. Statistical significance was determined using the unpaired t test.

inside the TME (Figure 6D). Subsampling the monocyte/macrophage subset revealed a distinct localization pattern for different subsets of macrophages; *Retnla^{H1}* macrophages were exclusively found at the outer regions of the TME, while *Apoe^{H1}*, *Ms4a7^{H1}*, and proliferating macrophages are skewed toward the interior of the TME (Figure 6E).

In line with our previous data obtained using orthotopic implantation of MMTV-PyMTChOVA-derived breast cancer cells (Hu et al., 2020), we found that CD8⁺ T cells have an increased exhaustion score (Wherry et al., 2007) when located in the inner regions of the TME (Figure 6F, left). Moreover, we applied pseudotime analysis (Cao et al., 2019) on the monocyte/macrophage subset, and specified the *Ly6c2^{H1}* monocyte-like cells as the root state of the trajectory, which resulted in the *Apoe^{H1}*, *Ms4a7^{H1}* and proliferating macrophages as the terminal states (Figures S6D and S6E), consistent with our previous findings (Hu et al., 2020; Mujal et al., 2022). When we overlaid ZipSeq spatial localization on our pseudotime trajectory, we found a correlation with pseudotime progressing from monocyte-like early states at the outer regions to terminally differentiated TAM states in the tumor core (Figure S6F). This was also reflected in an advanced monocyte/macrophage pseudotime score when moving from the exterior toward the interior of the tumor (Figure 6G, left). Interestingly, the positive correlation between the expression of exhaustion-related genes in CD8⁺ T cells and macrophage maturation toward the inner regions of the TME coincided with an increased glycolytic score (Argüello et al., 2020) in CD8⁺ T cells, but not in the monocyte/macrophage fraction (Figures 6F, right, and 6G, right), consistent with a more hypoxic microenvironment, which correlates with this dysfunctional crosstalk between T_{ex} and TAMs.

To predict the interaction likelihood between different cell types in distinct regions in the TME, we used CellChat analysis, which uses a curated database of receptor-ligand interactions to highlight likely cell-cell interactions (Jin et al., 2021). These analyses revealed that expression of the CSF1-CSF1R ligand-receptor pair is significantly enriched in likelihood, and especially in the inner region versus the outer region of tumors (Figure 6H). Interestingly, *Csf1* is found to be exclusively expressed by T_{ex} in those regions (Figure 6H). CellChat analysis also predicted that the main receivers of T_{ex}-derived *Csf1* in the inner regions of the tumor are *Ms4a7^{H1}* macrophages, proliferating macrophages, and *Apoe^{H1}* macrophages (Figure 6H), pointing toward a co-dependency between TAMs and T_{ex}. In line with this, we found a positive correlation between an “exhaustion” signature, as well as normalized *Csf1* and *Ccl4* expression in CD8⁺ T cells and macrophage maturation (monocyte/macrophage pseudotime score), when moving from the outer toward the inner regions of the tumor (Figure 6I). Conversely, the expression of genes associated with antigen presentation in monocyte/macrophages gradually decreased when moving closer to the inner regions of

the tumor (Figure 6I). These data support a model in which monocytes, as they move inward and differentiate toward terminal TAM, downregulate antigen presentation in concert with the development of the exhausted state in T cells.

DISCUSSION

We mechanistically dissected a cellular co-alignment by which TAMs and CD8⁺ T_{ex} in the TME coexist in a self-enforcing positive feedback loop in mouse and human cancers. This includes finding that the secretion of growth factors and chemokines by one induces the other, the key interaction biology—a weakly stimulatory, yet long-duration synapse that primes T cells for exhaustion—and spatial transcriptomics that demonstrate the co-evolution of these differentiated cell states, across space, in tumor tissue. This demonstrates a principle of co-evolution of immunosuppressive cell types in the TME that supports immune evasion rather than destruction of the tumor.

The presence of TAMs in solid tumors often correlates with poor prognosis and failure of response to anticancer therapies (Zhang et al., 2012; De Palma and Lewis, 2013). These findings are consistent with the established role of TAMs in suppressing antitumor T cell immunity (DeNardo and Ruffell, 2019), and recent scRNA-seq studies and other immune profiling approaches have hinted at a potential link between the presence of TAMs and CD8⁺ T_{ex} in several different cancer types (Bi et al., 2021; Braun et al., 2021; Combes et al., 2022; Hong et al., 2021; Hu et al., 2020; Mujal et al., 2022; O’Connell et al., 2021; Wagner et al., 2019). However, these computational predictions require experimental investigation to establish causality. Building on previous findings from our own lab and others that CD8⁺ T cells preferentially localize in TAM-rich areas in the TME (Boissonnas et al., 2013; Boldajipour et al., 2016; Broz et al., 2014; Engelhardt et al., 2012; Peranzoni et al., 2018), we show here that the evolution of these long considered immunosuppressive cell types in the TME is extensively linked in a causal circuit.

Macrophages are known to display a remarkable heterogeneity and plasticity that is dependent on a variety of environmental cues, some of which are derived from T cells (DeNardo and Ruffell, 2019; Guerriero, 2019). However, before our study, a role for T_{ex} in shaping macrophage phenotype and function had not been reported. We find in our models that intratumoral T_{ex} are the main immune population producing macrophage-related factors to actively recruit monocytes and modulate their differentiation trajectory favoring antigen presentation. In our data, *Csf1* is a predominant and consistent “exhaustion” gene, and previous reports have identified *Ccl3*, *Ccl4*, and *Ccl5* as among the most differentially expressed genes in chronic viral infection-associated exhaustion (Wherry et al., 2007). Interestingly, we find that *Flt3L*, an important cytokine for CD103⁺

(D) Immunofluorescence of B78ChOVA melanomas stained with pimonidazole (hypoxyprobe) Pacific blue, CD11b-AF594 (yellow), and CD31-AF647 (red). Scale bar, 100 μm. Scale bar inset, 50 μm.

(E) Average expression of hypoxia-related genes in T_{eff} (black), T_{ex} d4 (blue), and T_{ex} d14 (red) normalized to T_{naive} as determined by RNA-seq.

(F and G) Representative histograms (F) and quantification (G) of hypoxyprobe staining in CD45[−] cells, CD44⁺ OT-I CD8⁺ T cells, and CD11b⁺F4/80⁺ TAMs in B78ChOVA melanomas treated with isotype (black) or anti-CSF1R antibodies (blue). Statistical significance was determined using the Mann-Whitney U test. n = 4–5 mice/group. Representative of 2 independent experiments. All of the data are means ± SEMs; *p < 0.05, **p < 0.01, ***p < 0.001, ****p < 0.0001.

See also Figure S5.

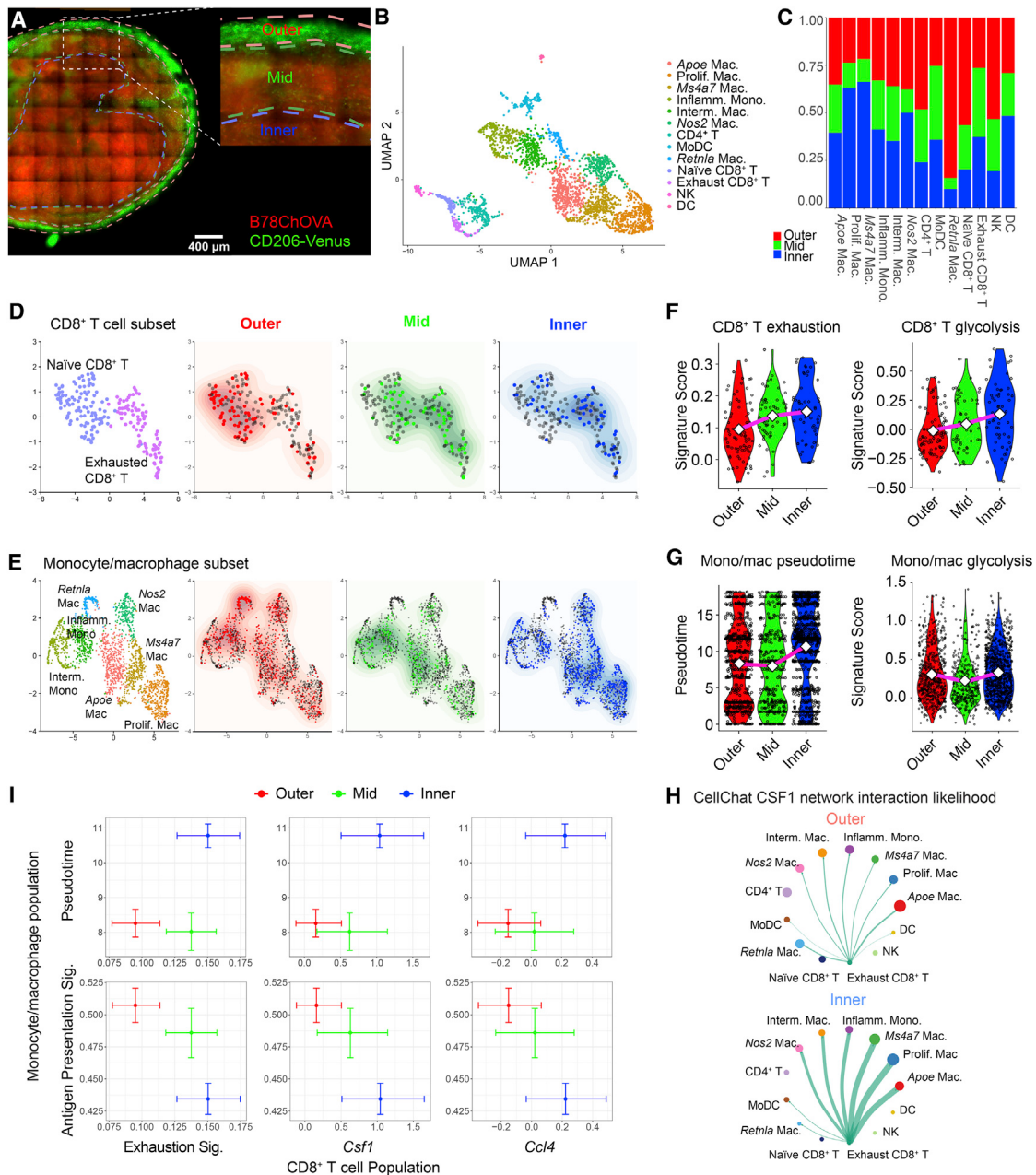


Figure 6. Spatial delineation of TAM-T_{ex} interaction dynamics in the TME

(A) Imaging of a 150- μ m-thick live B78ChOVA melanoma section, with ROI demarcation of outer, mid-, and inner compartments used for subsequent ZipSeq. Red channel denotes mCherry signal from B78ChOVA cancer cells and green channel indicates expression of mVenus in CD206⁺ macrophages in the *Csf1R*^{Cre};L_SL-Cd206-Venus-DTR mouse model. Scale bar, 400 μ m.

(B) UMAP representation of sorted CD45⁺ cells following 10X Genomics scRNA-seq workflow (n = 2,765 cells, with n = 427/394/335/288/275/244/220/170/120/108/91/62/31 for clusters as listed).

(C) Stacked bar charts representing regional distribution of distinct populations identified in (B).

(D) and (E) UMAP of subsampled CD8⁺ T cell subset ($n = 199$ cells) (D) and monocyte/macrophage subset ($n = 2,083$ cells) (E) overlaid with their regional localization.

(F) Violin plots representing CD8⁺ T cell exhaustion score (left; outer: 0.31/0.10/-0.07; mid: 0.35/0.14/-0.05; inner: 0.32/0.15/-0.01) and CD8⁺ T cell glycolytic score (right; outer: 0.45/-0.01/-0.37; mid: 0.60/0.05/-0.31; inner: 0.69/0.14/-0.45) in distinct regions in the TMF. Values max/average (diamond)/min

(G) Violin plots representing monocyte/macrophage pseudotime signature score (left; outer: 18.1/8.3/0.00; mid: 18.1/8.0/0.00; inner: 18.1/10.0/0.00) and monocyte/macrophage glycolytic score (right; outer: 1.35/0.29/-0.33; mid: 1.39/0.21/-0.33; inner: 1.39/0.33/-0.33). Values max/average (diamond)/min.

(H) CellChat interaction likelihood analysis for CSF1 network in outer (top) and inner (bottom) regions of the TME. Thickness of green arrows represents interaction likelihood between populations.

(legend continued on next page)
Cancer Cell 40, 624–638, June 13, 2022 633

cDC1 biology (Barry et al., 2018), is concurrently downregulated in T_{ex}, suggesting that upon progression to exhaustion, CD8⁺ T cells specifically favor the recruitment of TAMs (and not cDC1) to support their presence in the TME and prevent destruction of the tumor. We consider it likely that T_{ex} express additional myeloid-modulating factors that have yet to be identified and may now be sought, based on these studies. In addition, other cell types in the TME, including tumor cells and fibroblasts, can modulate myeloid biology through the secretion of a variety of cytokines (Buechler et al., 2021), and thus there may be settings in which additional cell types also contribute to the establishment of the TAM-T_{ex} axis.

Computational analysis of our spatial ZipSeq data suggests that T_{ex}-derived CSF1 is the most likely to affect specific subpopulations of terminally differentiated macrophages that are enriched in the inner regions of the TME, including Ms4a7^{H1}, Apoe^{H1}, and proliferating TAMs. While other scRNA-seq studies have also reported on the existence of multiple different subpopulations of monocytes and TAMs in the TME (Hu et al., 2020; Katzenellenbogen et al., 2020; Molgora et al., 2020; Mujal et al., 2022), it remains to be determined whether the localization in the TME affects their polarization state. Moreover, future studies will have to determine whether these subpopulations are functionally distinct from one another in their interactions with CD8⁺ T cells and their ability to modulate the onset of T cell exhaustion, and how other spatially regulated factors may play a role in the occurrence of TAM-T cell interactions.

Regardless of their ability to phagocytose large amounts of antigen, TAM are often considered inferior in antigen processing and presentation as compared to conventional DCs. Here, we show that antigen-presenting TAMs capture CD8⁺ T cells in uniquely long-lasting synaptic interactions characterized by the formation of variegated TCR microclusters. Despite expressing similar levels of MHC classes I and II, co-stimulatory molecules, and genes involved in cross-presentation as does cDC1 (Broz et al., 2014), TAMs trigger only a weak TCR stimulation that fails to support proliferation, but clearly primes the onset of T cell exhaustion, which is not observed in the absence of TCR ligands presented by these TAMs. Notably, the blockade of immune checkpoint molecules PD-1/PD-L1 and CTLA-4 is unable to license proliferation in T cells responding to TAMs (Engelhardt et al., 2012). It is clear that more work is required to better understand the fundamental nature of disparate TCR triggers and co-stimulation over time that contribute to the hyporesponsive state in T cells during tumorigenesis, as elegantly reviewed recently (Philip and Schietinger, 2021).

Recent studies have reported that the development of T cell exhaustion during chronic infection and cancer occurs in a multistep fashion, revealing distinct subtypes with unique transcriptional and epigenetic dynamics, as well as their ability to respond to immune checkpoint blockade (Im et al., 2016; Philip et al., 2017; Satpathy et al., 2019; Siddiqui et al., 2019; Jansen et al., 2019; Miller et al., 2019; Beltra et al., 2020; Pritykin et al., 2021). The decision-making during this bifurcative process

seems to be tightly regulated by transcription factors such as IRF4 (Utzschneider et al., 2020; Chen et al., 2021; Seo et al., 2021), which we find is strongly upregulated by TAM despite only subtle other signs of TCR engagement. Furthermore, our *in vitro* co-culture studies suggest that TAMs at least are capable of mediating the early stages of exhaustion, which is exacerbated in hypoxic conditions. Hypoxia was recently shown to be an important co-factor in the induction of exhaustion *in vitro* (Scharping et al., 2021), and ZipSeq transcriptomics place terminal exhaustion *in vivo* preferentially in hypoxic regions of the TME. In line with this, other recent studies have elegantly demonstrated how metabolic insufficiencies drive mitochondrial stress in T cells contributing to exhaustion phenotypes in chronic infections and cancer (Bengsch et al., 2016; Thommen et al., 2018; Vardhana et al., 2020; Scharping et al., 2021). Future studies are required to determine whether the induction of exhaustion programs in CD8⁺ T cells is spatially coordinated, for example, through specialized TAM-rich niches in the TME.

Taken together, our work dissects a spatiotemporal co-evolution between CD8⁺ T_{ex} and TAMs in the TME that supports immune evasion rather than tumor destruction. We believe that co-dependency of different lineages may explain some of the resistance of the TME to targeting—removing just one cell population will still leave the other, to influence re-establishment of the targeted one. Thus, therapeutic strategies may need to break the biology underlying the TAM-T_{ex} axis at multiple points. Doing so may work in conjunction with existing immunotherapies to enhance antitumor immunity, and thereby expand the proportion of cancer patients who benefit from immunotherapies.

STAR METHODS

Detailed methods are provided in the online version of this paper and include the following:

- **KEY RESOURCES TABLE**
- **RESOURCE AVAILABILITY**
 - Lead contact
 - Materials availability
 - Data and code availability
- **EXPERIMENTAL MODEL AND SUBJECT DETAILS**
 - Human tumor samples
 - Mice
 - Tumor cell lines
- **METHOD DETAILS**
 - Tumor growth experiments
 - Adoptive T cell transfers
 - *In vivo* antibody treatment
 - Generation of mixed bone marrow chimeras
 - Mouse tissue digestion and flow cytometry
 - Fluorescence activated cell sorting
 - Intracellular T cell cytokine analysis
 - ELISA and Cytometric Bead Array
 - RNA sequencing

(I) Cross-whisker plots comparing expression of exhaustion signature and normalized single gene (*Csf1* and *Ccl4*) expression in CD8⁺ T cells (x axis), and pseudotime score and antigen-presentation signature in the monocyte/macrophage population (y axis) in distinct regions in the TME. Error bars represent 95% confidence interval (CI) as computed by bootstrap resampling.
See also Figure S6 and Table S1.

- ATAC sequencing
- qRT-PCR
- Monocyte recruitment transwell assays
- Generation of activated T cells
- Bone marrow-derived dendritic cells
- Quantification of APC-T cell interactions
- APC-T cell coupling assay
- Lattice light-sheet imaging
- FURA-2AM calcium imaging
- Hypoxyprobe imaging
- *In vitro* APC-T cell co-culture assays
- ZipSeq
- Analysis of scRNA-Seq

● QUANTIFICATION AND STATISTICAL ANALYSIS

- Statistical analysis

SUPPLEMENTAL INFORMATION

Supplemental information can be found online at <https://doi.org/10.1016/j.ccel.2022.05.004>.

ACKNOWLEDGMENTS

We thank all of the members of the Krummel laboratory for discussion and support. We also thank the ImmunoX CoLabs at UCSF for technical assistance and support. Figures were created using [BioRender.com](#). K.K. was supported by Rubicon postdoctoral fellowship 019.163LW.006 from the Netherlands Organisation for Scientific Research, and a Parker Scholar Award from the Parker Institute for Cancer Immunotherapy. K.H.H. was supported by a Parker Scholar Award from the Parker Institute for Cancer Immunotherapy, and a Jean Perkins postdoctoral fellowship from the American Cancer Society. A.R. and E.C. were supported by postdoctoral fellowships from the Cancer Research Institute. J.B. was supported by a Stanford Graduate Fellowship and the National Science Foundation Graduate Research Fellowship under grant no. DGE-1656518. A.T.S. was supported by NIH U01CA260852, a Cancer Research Institute Technology Impact Award, and a Career Award for Medical Scientists from the Burroughs Wellcome Fund. We acknowledge the UCSF Parnassus Flow Core (RRID: SCR_018206 and DRC Center grant NIH P30 DK063720) for assistance and the use of their instruments and services. This work was supported by NIH/NCI U54CA163123, 5U01CA217864, R21CA191428, and R01CA197363, to M.F.K.

AUTHOR CONTRIBUTIONS

K.K. designed and conducted most of the experiments and data analysis and drafted the manuscript. K.H.H. and A.R. designed, performed, and analyzed the ZipSeq experiments. A.J.C. and B.S. analyzed the human cancer patient datasets. T.H. assisted with the co-culture experiments. A.A.R. analyzed the RNA-seq data. E.C., K.M., and J.A. provided technical support and assisted with the imaging experiments. T.C. discussed the data and project direction. Q.S., J.B., and A.T.S. performed ATAC-seq and assisted with the data analysis. M.F.K. designed the experiments, interpreted the data, and, with other co-authors, developed the manuscript.

DECLARATION OF INTERESTS

A.T.S. is a scientific founder of Immunai and founder of Cartography Biosciences and receives research funding from Merck Research Laboratories and Allogene Therapeutics. M.F.K. is a founder and shareholder in Pionyr Immunotherapeutics and in Foundry Innovations, which prosecute and develop novel immunotherapeutics, respectively. The other authors declare no competing interests.

INCLUSION AND DIVERSITY

One or more of the authors of this paper self-identifies as living with a disability.

Received: October 8, 2021

Revised: February 8, 2022

Accepted: May 4, 2022

Published: May 26, 2022

REFERENCES

- Alfei, F., Kanev, K., Hofmann, M., Wu, M., Ghoneim, H.E., Roelli, P., Utzschneider, D.T., von Hoesslin, M., Cullen, J.G., Fan, Y., et al. (2019). TOX reinforces the phenotype and longevity of exhausted T cells in chronic viral infection. *Nature* 571, 265–269. <https://doi.org/10.1038/s41586-019-1326-9>.
- Argüello, R.J., Combes, A.J., Char, R., Gigan, J.-P., Baaziz, A.I., Bousiquot, E., Camosseto, V., Samad, B., Tsui, J., Yan, P., et al. (2020). SCENITH: a flow cytometry-based method to functionally profile energy metabolism with single-cell resolution. *Cell Metab* 32, 1063–1075.e7. <https://doi.org/10.1016/j.cmet.2020.11.007>.
- Barry, K.C., Hsu, J., Broz, M.L., Cueto, F.J., Binnewies, M., Combes, A.J., Nelson, A.E., Loo, K., Kumar, R., Rosenblum, M.D., et al. (2018). A natural killer-dendritic cell axis defines checkpoint therapy-responsive tumor microenvironments. *Nat. Med.* 24, 1178–1191. <https://doi.org/10.1038/s41591-018-0085-8>.
- Beatty, G.L., Chiorean, E.G., Fishman, M.P., Saboury, B., Teitelbaum, U.R., Sun, W., Huhn, R.D., Song, W., Li, D., Sharp, L.L., et al. (2011). CD40 agonists alter tumor stroma and show efficacy against pancreatic carcinoma in mice and humans. *Science* 331, 1612–1616. <https://doi.org/10.1126/science.1198443>.
- Beltra, J.-C., Manne, S., Abdel-Hakeem, M.S., Kurachi, M., Giles, J.R., Chen, Z., Casella, V., Ngiow, S.F., Khan, O., Huang, Y.J., et al. (2020). Developmental relationships of four exhausted CD8+ T cell subsets reveals underlying transcriptional and epigenetic landscape control mechanisms. *Immunity* 52, 825–841.e8. <https://doi.org/10.1016/j.immuni.2020.04.014>.
- Bengsch, B., Johnson, A.L., Kurachi, M., Odorizzi, P.M., Pauken, K.E., Attanasio, J., Stelekati, E., McLane, L.M., Paley, M.A., Delgoffe, G.M., and Wherry, E.J. (2016). Bioenergetic insufficiencies due to metabolic alterations regulated by the inhibitory receptor PD-1 are an early driver of CD8(+) T cell exhaustion. *Immunity* 45, 358–373. <https://doi.org/10.1016/j.immuni.2016.07.008>.
- Bi, K., He, M.X., Bakouny, Z., Kanodia, A., Napolitano, S., Wu, J., Grimaldi, G., Braun, D.A., Cuoco, M.S., Mayorga, A., et al. (2021). Tumor and immune reprogramming during immunotherapy in advanced renal cell carcinoma. *Cancer Cell* 39, 649–661.e5. <https://doi.org/10.1016/j.ccr.2021.02.015>.
- Binnewies, M., Roberts, E.W., Kersten, K., Chan, V., Fearon, D.F., Merad, M., Coussens, L.M., Gabrilovich, D.I., Ostrand-Rosenberg, S., Hedrick, C.C., et al. (2018). Understanding the tumor immune microenvironment (TIME) for effective therapy. *Nat. Med.* 24, 541–550. <https://doi.org/10.1038/s41591-018-0014-x>.
- Binnewies, M., Mujal, A.M., Pollack, J.L., Combes, A.J., Hardison, E.A., Barry, K.C., Tsui, J., Ruhland, M.K., Kersten, K., Abushawish, M.A., et al. (2019). Unleashing type-2 dendritic cells to drive protective antitumor CD4+ T cell immunity. *Cell* 177, 556–571.e16. <https://doi.org/10.1016/j.cell.2019.02.005>.
- Boissonnas, A., Licata, F., Poupel, L., Jacquelin, S., Fetler, L., Krumeich, S., Théry, C., Amigorena, S., and Combadière, C. (2013). CD8+ tumor-infiltrating T cells are trapped in the tumor-dendritic cell network. *Neoplasia* 15, 85–94. <https://doi.org/10.1593/neo.121572>.
- Boldajipour, B., Nelson, A., and Krummel, M.F. (2016). Tumor-infiltrating lymphocytes are dynamically desensitized to antigen but are maintained by homeostatic cytokine. *JCI Insight* 1, e89289. <https://doi.org/10.1172/jci.insight.89289>.
- Braun, D.A., Street, K., Burke, K.P., Cookmeyer, D.L., Denize, T., Pedersen, C.B., Gohil, S.H., Schindler, N., Pomerance, L., Hirsch, L., et al. (2021). Progressive immune dysfunction with advancing disease stage in renal cell carcinoma. *Cancer Cell* 39, 632–648.e8. <https://doi.org/10.1016/j.ccr.2021.02.013>.
- Broz, M.L., Binnewies, M., Boldajipour, B., Nelson, A.E., Pollack, J.L., Erle, D.J., Barczak, A., Rosenblum, M.D., Daud, A., Barber, D.L., et al. (2014).

- Dissecting the tumor myeloid compartment reveals rare activating antigen-presenting cells critical for T cell immunity. *Cancer Cell* 26, 638–652. <https://doi.org/10.1016/j.ccr.2014.09.007>.
- Buechler, M.B., Fu, W., and Turley, S.J. (2021). Fibroblast-macrophage reciprocal interactions in health, fibrosis, and cancer. *Immunity* 54, 903–915. <https://doi.org/10.1016/j.immuni.2021.04.021>.
- Cai, E., Marchuk, K., Beemiller, P., Beppeler, C., Rubashkin, M.G., Weaver, V.M., Gérard, A., Liu, T.-L., Chen, B.-C., Betzig, E., et al. (2017). Visualizing dynamic microvillar search and stabilization during ligand detection by T cells. *Science* 356, eaal3118. <https://doi.org/10.1126/science.aal3118>.
- Cao, J., Spielmann, M., Qiu, X., Huang, X., Ibrahim, D.M., Hill, A.J., Zhang, F., Mundlos, S., Christiansen, L., Steemers, F.J., et al. (2019). The single-cell transcriptional landscape of mammalian organogenesis. *Nature* 566, 496–502. <https://doi.org/10.1038/s41586-019-0969-x>.
- Chen, E.Y., Tan, C.M., Kou, Y., Duan, Q., Wang, Z., Meirelles, G.V., Clark, N.R., and Ma'ayan, A. (2013). Enrichr: interactive and collaborative HTML5 gene list enrichment analysis tool. *BMC Bioinformatics* 14, 128. <https://doi.org/10.1186/1471-2105-14-128>.
- Chen, S., Zhou, Y., Chen, Y., and Gu, J. (2018). fastp: an ultra-fast all-in-one FASTQ preprocessor. *Bioinformatics* 34, i884–i890. <https://doi.org/10.1093/bioinformatics/bty560>.
- Chen, Y., Zander, R.A., Wu, X., Schauder, D.M., Kasmani, M.Y., Shen, J., Zheng, S., Burns, R., Taparowsky, E.J., and Cui, W. (2021). BATF regulates progenitor to cytolytic effector CD8+ T cell transition during chronic viral infection. *Nat. Immunol.* 22, 996–1007. <https://doi.org/10.1038/s41590-021-00965-7>.
- Cheng, S., Li, Z., Gao, R., Xing, B., Gao, Y., Yang, Y., Qin, S., Zhang, L., Ouyang, H., Du, P., et al. (2021). A pan-cancer single-cell transcriptional atlas of tumor infiltrating myeloid cells. *Cell* 184, 792–809.e23. <https://doi.org/10.1016/j.cell.2021.01.010>.
- Combes, A.J., Samad, B., Tsui, J., Chew, N.W., Yan, P., Reeder, G.C., Kushnoor, D., Shen, A., Davidson, B., Barczak, A.J., et al. (2022). Discovering dominant tumor immune archetypes in a pan-cancer census. *Cell* 185, 184–203.e19. <https://doi.org/10.1016/j.cell.2021.12.004>.
- Corces, M.R., Trevino, A.E., Hamilton, E.G., Greenside, P.G., Sinnott-Armstrong, N.A., Vesuna, S., Satpathy, A.T., Rubin, A.J., Montine, K.S., Wu, B., et al. (2017). An improved ATAC-seq protocol reduces background and enables interrogation of frozen tissues. *Nat. Methods* 14, 959–962. <https://doi.org/10.1038/nmeth.4396>.
- Corces, M.R., Granja, J.M., Shams, S., Louie, B.H., Seoane, J.A., Zhou, W., Silva, T.C., Groeneveld, C., Wong, C.K., Cho, S.W., et al. (2018). The chromatin accessibility landscape of primary human cancers. *Science* 362, eaav1898. <https://doi.org/10.1126/science.aav1898>.
- De Palma, M., and Lewis, C.E. (2013). Macrophage regulation of tumor responses to anticancer therapies. *Cancer Cell* 23, 277–286. <https://doi.org/10.1016/j.ccr.2013.02.013>.
- DeNardo, D.G., and Ruffell, B. (2019). Macrophages as regulators of tumour immunity and immunotherapy. *Nat. Rev. Immunol.* 19, 369–382. <https://doi.org/10.1038/s41577-019-0127-6>.
- DeNardo, D.G., Brennan, D.J., Rexhepaj, E., Ruffell, B., Shiao, S.L., Madden, S.F., Gallagher, W.M., Wadhwan, N., Keil, S.D., Junaid, S.A., et al. (2011). Leukocyte complexity predicts breast cancer survival and functionally regulates response to chemotherapy. *Cancer Discov.* 1, 54–67. <https://doi.org/10.1158/2159-8274.CD-10-0028>.
- Dobin, A., Davis, C.A., Schlesinger, F., Drenkow, J., Zaleski, C., Jha, S., Batut, P., Chaisson, M., and Gingeras, T.R. (2013). STAR: ultrafast universal RNA-seq aligner. *Bioinformatics* 29, 15–21. <https://doi.org/10.1093/bioinformatics/bts635>.
- Doering, T.A., Crawford, A., Angelosanto, J.M., Paley, M.A., Ziegler, C.G., and Wherry, E.J. (2012). Network analysis reveals centrally connected genes and pathways involved in CD8+ T cell exhaustion versus memory. *Immunity* 37, 1130–1144. <https://doi.org/10.1016/j.immuni.2012.08.021>.
- Engelhardt, J.J., Boldajipour, B., Beemiller, P., Pandurangi, P., Sorensen, C., Werb, Z., Egeblad, M., and Krummel, M.F. (2012). Marginating dendritic cells of the tumor microenvironment cross-present tumor antigens and stably engage tumor-specific T cells. *Cancer Cell* 21, 402–417. <https://doi.org/10.1016/j.ccr.2012.01.008>.
- Frankish, A., Diekhans, M., Ferreira, A.-M., Johnson, R., Jungreis, I., Loveland, J., Mudge, J.M., Sisu, C., Wright, J., Armstrong, J., et al. (2019). GENCODE reference annotation for the human and mouse genomes. *Nucleic Acids Res.* 47, D766–D773. <https://doi.org/10.1093/nar/gky955>.
- Galon, J., Costes, A., Sanchez-Cabo, F., Kirilovsky, A., Mlecnik, B., Lagorce-Pagès, C., Tosolini, M., Camus, M., Berger, A., Wind, P., et al. (2006). Type, density, and location of immune cells within human colorectal tumors predict clinical outcome. *Science* 313, 1960–1964. <https://doi.org/10.1126/science.1129139>.
- Gentles, A.J., Newman, A.M., Liu, C.L., Bratman, S.V., Feng, W., Kim, D., Nair, V.S., Xu, Y., Khuong, A., Hoang, C.D., et al. (2015). The prognostic landscape of genes and infiltrating immune cells across human cancers. *Nat. Med.* 21, 938–945. <https://doi.org/10.1038/nm.3909>.
- Guerriero, J.L. (2019). Macrophages. *Int. Rev. Cell Mol. Biol.* 342, 73–93. <https://doi.org/10.1016/bs.ircmb.2018.07.001>.
- Hafemeister, C., and Satija, R. (2019). Normalization and variance stabilization of single-cell RNA-seq data using regularized negative binomial regression. *Genome Biol.* 20, 296. <https://doi.org/10.1186/s13059-019-1874-1>.
- Hong, F., Meng, Q., Zhang, W., Zheng, R., Li, X., Cheng, T., Hu, D., and Gao, X. (2021). Single-cell analysis of the pan-cancer immune microenvironment and scTIME portal. *Cancer Immunol. Res.* 9, 939–951. <https://doi.org/10.1158/2326-6066.CIR-20-1026>.
- Hu, K.H., Eichorst, J.P., McGinnis, C.S., Patterson, D.M., Chow, E.D., Kersten, K., Jameson, S.C., Gartner, Z.J., Rao, A.A., and Krummel, M.F. (2020). ZipSeq: barcoding for real-time mapping of single cell transcriptomes. *Nat. Methods* 17, 833–843. <https://doi.org/10.1038/s41592-020-0880-2>.
- Im, S.J., Hashimoto, M., Gerner, M.Y., Lee, J., Kissick, H.T., Burger, M.C., Shan, Q., Hale, J.S., Lee, J., Nasti, T.H., et al. (2016). Defining CD8+ T cells that provide the proliferative burst after PD-1 therapy. *Nature* 537, 417–421. <https://doi.org/10.1038/nature19330>.
- Jansen, C.S., Prokhnovska, N., Master, V.A., Sanda, M.G., Carlisle, J.W., Bilen, M.A., Cardenas, M., Wilkinson, S., Lake, R., Sowalsky, A.G., et al. (2019). An intra-tumoral niche maintains and differentiates stem-like CD8 T cells. *Nature* 576, 465–470. <https://doi.org/10.1038/s41586-019-1836-5>.
- Jin, S., Guerrero-Juarez, C.F., Zhang, L., Chang, I., Ramos, R., Kuan, C.-H., Myung, P., Plikus, M.V., and Nie, Q. (2021). Inference and analysis of cell-cell communication using CellChat. *Nat. Commun.* 12, 1088. <https://doi.org/10.1038/s41467-021-21246-9>.
- Katzenellenbogen, Y., Sheban, F., Yalin, A., Yofe, I., Svetlichnyy, D., Jaitin, D.A., Bornstein, C., Moshe, A., Keren-Shaul, H., Cohen, M., et al. (2020). Coupled scRNA-seq and intracellular protein activity reveal an immunosuppressive role of TREM2 in cancer. *Cell* 182, 872–885.e19. <https://doi.org/10.1016/j.cell.2020.06.032>.
- Khan, O., Giles, J.R., McDonald, S., Manne, S., Ngiow, S.F., Patel, K.P., Werner, M.T., Huang, A.C., Alexander, K.A., Wu, J.E., et al. (2019). TOX transcriptionally and epigenetically programs CD8 + T cell exhaustion. *Nature* 571, 211–218. <https://doi.org/10.1038/s41586-019-1325-x>.
- Klug, F., Prakash, H., Huber, P.E., Seibel, T., Bender, N., Halama, N., Pfirsichke, C., Voss, R.H., Timke, C., Umansky, L., et al. (2013). Low-dose irradiation programs macrophage differentiation to an iNOS+/M1 phenotype that orchestrates effective T cell immunotherapy. *Cancer Cell* 24, 589–602. <https://doi.org/10.1016/j.ccr.2013.09.014>.
- Kuleshov, M.V., Jones, M.R., Rouillard, A.D., Fernandez, N.F., Duan, Q., Wang, Z., Koplev, S., Jenkins, S.L., Jagodnik, K.M., Lachmann, A., et al. (2016). Enrichr: a comprehensive gene set enrichment analysis web server 2016 update. *Nucleic Acids Res.* 44, W90–W97. <https://doi.org/10.1093/nar/gkw377>.
- Law, C.W., Chen, Y., Shi, W., and Smyth, G.K. (2014). voom: precision weights unlock linear model analysis tools for RNA-seq read counts. *Genome Biol.* 15, R29. <https://doi.org/10.1186/gb-2014-15-2-r29>.

- Man, K., Gabriel, S.S., Liao, Y., Glourey, R., Preston, S., Henstridge, D.C., Pellegrini, M., Zehn, D., Berberich-Siebelt, F., Febbraio, M.A., et al. (2017). Transcription factor IRF4 promotes CD8+ T cell exhaustion and limits the development of memory-like T cells during chronic infection. *Immunity* 47, 1129–1141.e5. <https://doi.org/10.1016/j.immuni.2017.11.021>.
- Miller, B.C., Sen, D.R., Al Abosy, R., Bi, K., Virkud, Y.V., LaFleur, M.W., Yates, K.B., Lako, A., Felt, K., Naik, G.S., et al. (2019). Subsets of exhausted CD8+ T cells differentially mediate tumor control and respond to checkpoint blockade. *Nat. Immunol.* 20, 326–336. <https://doi.org/10.1038/s41590-019-0312-6>.
- Molgora, M., Esaulova, E., Vermi, W., Hou, J., Chen, Y., Luo, J., Brioschi, S., Bugatti, M., Omodei, A.S., Ricci, B., et al. (2020). TREM2 modulation remodels the tumor myeloid landscape enhancing anti-PD-1 immunotherapy. *Cell* 182, 886–900.e17. <https://doi.org/10.1016/j.cell.2020.07.013>.
- Mujal, A.M., Combes, A.J., Rao, A.A., Binnewies, M., Samad, B., Tsui, J., Boissonnas, A., Pollack, J.L., Arguello, R.J., Meng, M.V., Porten, S.P., Ruhland, M.K., Barry, K.C., Chan, V., and Krummel, M.F. (2022). Holistic characterization of tumor monocyte-to-macrophage differentiation integrates distinct immune phenotypes in kidney cancer. *Cancer Immunol. Res. Canimm.* 10, 403–419. <https://doi.org/10.1158/2326-6066.CIR-21-0588>.
- O'Connell, P., Hyslop, S., Blake, M.K., Godbehere, S., Amalfitano, A., and Aldhamen, Y.A. (2021). SLAMF7 signaling reprograms T cells toward exhaustion in the tumor microenvironment. *J. Immunol.* 206, 193–205. <https://doi.org/10.4049/jimmunol.2000300>.
- Oliveira, G., Stromhaug, K., Klaeger, S., Kula, T., Frederick, D.T., Le, P.M., Forman, J., Huang, T., Li, S., Zhang, W., et al. (2021). Phenotype, specificity and avidity of antitumour CD8+ T cells in melanoma. *Nature* 596, 119–125. <https://doi.org/10.1038/s41586-021-03704-y>.
- Pauken, K.E., Sammons, M.A., Odorizzi, P.M., Manne, S., Godec, J., Khan, O., Drake, A.M., Chen, Z., Sen, D.R., Kurachi, M., et al. (2016). Epigenetic stability of exhausted T cells limits durability of reinvigoration by PD-1 blockade. *Science* 354, 1160–1165. <https://doi.org/10.1126/science.aaf2807>.
- Peranzoni, E., Lemoine, J., Vimeux, L., Feuillet, V., Barrin, S., Kantari-Mimoun, C., Bercovici, N., Guérin, M., Biton, J., Ouakrim, H., et al. (2018). Macrophages impede CD8 T cells from reaching tumor cells and limit the efficacy of anti-PD-1 treatment. *Proc. Natl. Acad. Sci. U S A.* 115, E4041–E4050. <https://doi.org/10.1073/pnas.1720948115>.
- Philip, M., and Schietinger, A. (2021). CD8+ T cell differentiation and dysfunction in cancer. *Nat. Rev. Immunol.* 22, 209–223. <https://doi.org/10.1038/s41577-021-00574-3>.
- Philip, M., Fairchild, L., Sun, L., Horste, E.L., Camara, S., Shakiba, M., Scott, A.C., Viale, A., Lauer, P., Merghoub, T., et al. (2017). Chromatin states define tumour-specific T cell dysfunction and reprogramming. *Nature* 545, 452–456. <https://doi.org/10.1038/nature22367>.
- Pritykin, Y., van der Veeken, J., Pine, A.R., Zhong, Y., Sahin, M., Mazutis, L., Pe'er, D., Rudensky, A.Y., and Leslie, C.S. (2021). A unified atlas of CD8 T cell dysfunctional states in cancer and infection. *Mol. Cell* 81, 2477–2493.e10. <https://doi.org/10.1016/j.molcel.2021.03.045>.
- Roberts, E.W., Broz, M.L., Binnewies, M., Headley, M.B., Nelson, A.E., Wolf, D.M., Kaisho, T., Bogunovic, D., Bhardwaj, N., and Krummel, M.F. (2016). Critical role for CD103+/CD141+ dendritic cells bearing CCR7 for tumor antigen trafficking and priming of T cell immunity in melanoma. *Cancer Cell* 30, 324–336. <https://doi.org/10.1016/j.ccr.2016.06.003>.
- Robinson, M.D., McCarthy, D.J., and Smyth, G.K. (2010). edgeR: a Bioconductor package for differential expression analysis of digital gene expression data. *Bioinformatics* 26, 139–140. <https://doi.org/10.1093/bioinformatics/btp616>.
- Ruffell, B., Au, A., Rugo, H.S., Esserman, L.J., Hwang, E.S., and Coussens, L.M. (2012). Leukocyte composition of human breast cancer. *Proc. Natl. Acad. Sci. U. S. A.* 109, 2796–2801. <https://doi.org/10.1073/pnas.1104303109>.
- Sade-Feldman, M., Yizhak, K., Bjorgaard, S.L., Ray, J.P., de Boer, C.G., Jenkins, R.W., Lieb, D.J., Chen, J.H., Frederick, D.T., Barzily-Rokni, M., et al. (2018). Defining T cell states associated with response to checkpoint immunotherapy in melanoma. *Cell* 175, 998–1013.e20. <https://doi.org/10.1016/j.cell.2018.10.038>.
- Salmon, H., Idoaga, J., Rahman, A., Leboeuf, M., Remark, R., Jordan, S., Casanova-Acebes, M., Khudynazarova, M., Agudo, J., Tung, N., et al. (2016). Expansion and activation of CD103+ dendritic cell progenitors at the tumor site enhances tumor responses to therapeutic PD-L1 and BRAF inhibition. *Immunity* 44, 924–938. <https://doi.org/10.1016/j.immuni.2016.03.012>.
- Satija, R., Farrell, J.A., Gennert, D., Schier, A.F., and Regev, A. (2015). Spatial reconstruction of single-cell gene expression data. *Nat. Biotechnol.* 33, 495–502. <https://doi.org/10.1038/nbt.3192>.
- Satpathy, A.T., Granja, J.M., Yost, K.E., Qi, Y., Meschi, F., McDermott, G.P., Olsen, B.N., Mumbach, M.R., Pierce, S.E., Corces, M.R., et al. (2019). Massively parallel single-cell chromatin landscapes of human immune cell development and intratumoral T cell exhaustion. *Nat. Biotechnol.* 37, 925–936. <https://doi.org/10.1038/s41587-019-0206-z>.
- Scharping, N.E., Rivadeneira, D.B., Menk, A.V., Vignali, P.D.A., Ford, B.R., Rittenhouse, N.L., Peralta, R., Wang, Y., Wang, Y., DePeaux, K., et al. (2021). Mitochondrial stress induced by continuous stimulation under hypoxia rapidly drives T cell exhaustion. *Nat. Immunol.* 22, 205–215. <https://doi.org/10.1038/s41590-020-00834-9>.
- Schietinger, A., Philip, M., Krisnawan, V.E., Chiu, E.Y., Delrow, J.J., Basom, R.S., Lauer, P., Brockstedt, D.G., Knoblaugh, S.E., Hämmерling, G.J., et al. (2016). Tumor-specific T cell dysfunction is a dynamic antigen-driven differentiation program initiated early during tumorigenesis. *Immunity* 45, 389–401. <https://doi.org/10.1016/j.immuni.2016.07.011>.
- Scott, A.C., Dündar, F., Zumbo, P., Chandran, S.S., Klebanoff, C.A., Shakiba, M., Trivedi, P., Menocal, L., Appleby, H., Camara, S., et al. (2019). TOX is a critical regulator of tumour-specific T cell differentiation. *Nature* 571, 270–274. <https://doi.org/10.1038/s41586-019-1324-y>.
- Seo, H., González-Avalos, E., Zhang, W., Ramchandani, P., Yang, C., Lio, C.-W.J., Rao, A., and Hogan, P.G. (2021). BATF and IRF4 cooperate to counter exhaustion in tumor-infiltrating CAR T cells. *Nat. Immunol.* 22, 983–995. <https://doi.org/10.1038/s41590-021-00964-8>.
- Siddiqui, I., Schaeuble, K., Chennupati, V., Fuertes Marraco, S.A., Calderon-Copete, S., Pais Ferreira, D., Carmona, S.J., Scarpellino, L., Gfeller, D., Pradervand, S., et al. (2019). Intratumoral Tcf1+PD-1+CD8+ T cells with stem-like properties promote tumor control in response to vaccination and checkpoint blockade immunotherapy. *Immunity* 50, 195–211.e10. <https://doi.org/10.1016/j.immuni.2018.12.021>.
- Smyth, G.K. (2005). Limma: linear models for microarray data. In *Bioinformatics and Computational Biology Solutions Using R and Bioconductor*, R. Gentleman, V.J. Carey, W. Huber, R.A. Irizarry, and S. Dudoit, eds. (Springer New York), pp. 397–420.
- Spranger, S., Dai, D., Horton, B., and Gajewski, T.F. (2017). Tumor-residing Batf3 dendritic cells are required for effector T cell trafficking and adoptive T cell therapy. *Cancer Cell* 31, 711–723.e4. <https://doi.org/10.1016/j.ccr.2017.04.003>.
- Thommen, D.S., Koelzer, V.H., Herzig, P., Roller, A., Trefny, M., Dimeloe, S., Kiiälainen, A., Hanhart, J., Schill, C., Hess, C., et al. (2018). A transcriptionally and functionally distinct PD-1+ CD8+ T cell pool with predictive potential in non-small-cell lung cancer treated with PD-1 blockade. *Nat. Med.* 24, 994–1004. <https://doi.org/10.1038/s41591-018-0057-z>.
- Tumeh, P.C., Harview, C.L., Yearley, J.H., Shintaku, I.P., Taylor, E.J.M., Robert, L., Chmielowski, B., Spasic, M., Henry, G., Ciobanu, V., et al. (2014). PD-1 blockade induces responses by inhibiting adaptive immune resistance. *Nature* 515, 568–571. <https://doi.org/10.1038/nature13954>.
- Utzschneider, D.T., Alfei, F., Roelli, P., Barras, D., Chennupati, V., Darbre, S., Delorenzi, M., Pinschewer, D.D., and Zehn, D. (2016). High antigen levels induce an exhausted phenotype in a chronic infection without impairing T cell expansion and survival. *J. Exp. Med.* 213, 1819–1834. <https://doi.org/10.1084/jem.20150598>.
- Utzschneider, D.T., Gabriel, S.S., Chisanga, D., Glourey, R., Gubser, P.M., Vasantha Kumar, A., Shi, W., and Kallies, A. (2020). Early precursor T cells establish and propagate T cell exhaustion in chronic infection. *Nat. Immunol.* 21, 1256–1266. <https://doi.org/10.1038/s41590-020-0760-z>.

- Vardhana, S.A., Hwee, M.A., Berisa, M., Wells, D.K., Yost, K.E., King, B., Smith, M., Herrera, P.S., Chang, H.Y., Satpathy, A.T., et al. (2020). Impaired mitochondrial oxidative phosphorylation limits the self-renewal of T cells exposed to persistent antigen. *Nat. Immunol.* 21, 1022–1033. <https://doi.org/10.1038/s41590-020-0725-2>.
- Wagner, J., Rapsomaniki, M.A., Chevrier, S., Anzeneder, T., Langwieder, C., Dykgers, A., Rees, M., Ramaswamy, A., Muenst, S., Soysal, S.D., et al. (2019). A single-cell atlas of the tumor and immune ecosystem of human breast cancer. *Cell* 177, 1330–1345.e18. <https://doi.org/10.1016/j.cell.2019.03.005>.
- Weber, E.W., Parker, K.R., Sotillo, E., Lynn, R.C., Anbunathan, H., Lattin, J., Good, Z., Belk, J.A., Daniel, B., Klysz, D., et al. (2021). Transient rest restores functionality in exhausted CAR-T cells through epigenetic remodeling. *Science* 372, eaba1786. <https://doi.org/10.1126/science.aba1786>.
- Wherry, E.J., Ha, S.-J., Kaech, S.M., Haining, W.N., Sarkar, S., Kalia, V., Subramaniam, S., Blattman, J.N., Barber, D.L., and Ahmed, R. (2007). Molecular signature of CD8+ T cell exhaustion during chronic viral infection. *Immunity* 27, 670–684. <https://doi.org/10.1016/j.immuni.2007.09.006>.
- Xie, Z., Bailey, A., Kuleshov, M.V., Clarke, D.J.B., Evangelista, J.E., Jenkins, S.L., Lachmann, A., Wojciechowicz, M.L., Kropiwnicki, E., Jagodnik, K.M., et al. (2021). Gene Set Knowledge Discovery with Enrichr. *Curr. Protoc.* 1, e90. <https://doi.org/10.1002/cpz1.90>.
- Yao, C., Sun, H.-W., Lacey, N.E., Ji, Y., Moseman, E.A., Shih, H.-Y., Heuston, E.F., Kirby, M., Anderson, S., Cheng, J., et al. (2019). Single-cell RNA-seq reveals TOX as a key regulator of CD8+ T cell persistence in chronic infection. *Nat. Immunol.* 20, 890–901. <https://doi.org/10.1038/s41590-019-0403-4>.
- Zhang, Q.w., Liu, L., Gong, C.y., Shi, H.s., Zeng, Y.h., Wang, X., Zhao, Y., Wei, Y.q., and Wei, Y. (2012). Prognostic significance of tumor-associated macrophages in solid tumor: a meta-analysis of the literature. *PLoS One* 7, e50946. <https://doi.org/10.1371/journal.pone.0050946>.

STAR★METHODS

KEY RESOURCES TABLE

REAGENT or RESOURCE	SOURCE	IDENTIFIER
Antibodies		
anti-mouse CD103 - BUV737 (clone 2E7)	BD BioSciences	Cat# 749393; RRID: AB_2873763
anti-mouse CD103 - PE (clone 2E7)	Biolegend	Cat# 121406; RRID: AB_1133989
anti-mouse CD103 - PerCp-Cy5.5 (clone 2E7)	Biolegend	Cat# 121416; RRID: AB_2128621
anti-mouse CD11b - AF594 (clone M1/70)	Biolegend	Cat# 101254; RRID: AB_2563231
anti-mouse CD11b - BV421 (clone M1/70)	Biolegend	Cat# 101235; RRID: AB_10897942
anti-mouse CD11b - BV605 (clone M1/70)	Biolegend	Cat# 101237; RRID: AB_11126744
anti-mouse CD11b - BV650 (clone M1/70)	Biolegend	Cat# 101239; RRID: AB_11125575
anti-mouse CD11b - BV785 (clone M1/70)	Biolegend	Cat# 101243; RRID: AB_2561373
anti-mouse CD11c - BV650 (clone N418)	Biolegend	Cat# 117339; RRID: AB_2562414
anti-mouse CD11c - PerCp-Cy5.5 (clone N418)	Biolegend	Cat# 117328; RRID: AB_2129641
anti-mouse CD206 - AF488 (clone C068C2)	Biolegend	Cat# 141710; RRID: AB_10900445
anti-mouse CD206 - PerCp-Cy5.5 (clone C068C2)	Biolegend	Cat# 141716; RRID: AB_2561992
anti-mouse CD24 - BV421 (clone M1/69)	Biolegend	Cat# 101825; RRID: AB_10901159
anti-mouse CD24 - PECy7 (clone M1/69)	Biolegend	Cat# 101822; RRID: AB_756048
anti-mouse CD31 - AF647 (clone 390)	Biolegend	Cat# 102415; RRID: AB_493411
anti-mouse CD38 - BV711 (clone 90/CD38)	BD BioSciences	Cat# 740697; RRID: AB_2740381
anti-mouse CD38 - FITC (clone 90/CD38)	BD BioSciences	Cat# 558813; RRID: AB_397126
anti-mouse CD4 - BUV395 (clone RM4-5)	BD BioSciences	Cat# 563790; RRID: AB_2738426
anti-mouse CD44 - BUV737 (clone IM7)	BD BioSciences	Cat# 564392; RRID: AB_2738785
anti-mouse CD44 - AF700 (clone IM7)	Thermo Fisher Scientific	Cat# 56-0441-80; RRID: AB_494012
anti-mouse CD45 AF647 (clone 30-F11)	Biolegend	Cat# 103124; RRID: AB_493533
anti-mouse CD45 - BUV395 (clone 30-F11)	BD BioSciences	Cat# 564279; RRID: AB_2651134
anti-mouse CD45 - BV421 (clone 30-F11)	Biolegend	Cat# 304032; RRID: AB_2561357
anti-mouse CD45.1 - BUV395 (clone A20)	BD BioSciences	Cat# 565212; RRID: AB_2722493
anti-mouse CD45.1 - PECy7 (clone A20)	Biolegend	Cat# 110730; RRID: AB_1134168
anti-mouse CD45R (B220) - BV785 (clone RA3-6B2)	Biolegend	Cat# 103245; RRID: AB_11218795
anti-mouse CD5 - BV510 (clone 53-7.3)	Biolegend	Cat# 100627; RRID: AB_2563930
anti-mouse CD69 - BV650 (clone H1.2F3)	Biolegend	Cat# 104541; RRID: AB_2616934
anti-mouse CD8 - AF488 (clone 53-6.7)	Biolegend	Cat# 100723; RRID: AB_389304
anti-mouse CD8 - PerCp-Cy5.5 (clone 53-6.7)	Biolegend	Cat# 100734; RRID: AB_2075238
anti-mouse CD80 - FITC (clone 16-10A1)	Thermo Fisher Scientific	Cat# 11-0801-82; RRID: AB_465133
anti-mouse CD86 - APC (clone GL-1)	Biolegend	Cat# 105012; RRID: AB_493342
anti-mouse CD86 - BV421 (clone GL-1)	Biolegend	Cat# 105031; RRID: AB_10898329
anti-mouse CD90.2 - AF700 (clone 30-H12)	Biolegend	Cat# 105320; RRID: AB_493725
anti-mouse CD90.2 - BV785 (clone 30-H12)	Biolegend	Cat# 105331; RRID: AB_2562900
anti-mouse CSF1R (CD115) - PECy7 (clone AFS98)	Biolegend	Cat# 135524; RRID: AB_2566460
anti-mouse F4/80 - AF700 (clone BM8)	Biolegend	Cat# 123130; RRID: AB_2293450
anti-mouse F4/80 - BV510 (clone BM8)	Biolegend	Cat# 123135; RRID: AB_2562622
anti-mouse H2kB - PE (clone AF6-88.5)	Biolegend	Cat# 116507; RRID: AB_313734
anti-mouse IFNy - PE (clone XMG1.2)	Thermo Fisher Scientific	Cat# 12-7311-81; RRID: AB_466192
anti-mouse IFNy - PECy7 (clone XMG1.2)	Biolegend	Cat# 505826; RRID: AB_2295770
anti-mouse IRF4 - FITC (clone 3E4)	Thermo Fisher Scientific	Cat# 11-9858-82; RRID: AB_2572538
anti-mouse IRF4 - PECy7 (clone 3E4)	Thermo Fisher Scientific	Cat# 25-9858-82; RRID: AB_2573558
anti-mouse Ki67 - PE eFluor610 (clone SolA15)	Thermo Fisher Scientific	Cat# 61-5698-82; RRID: AB_2574620

(Continued on next page)

Continued

REAGENT or RESOURCE	SOURCE	IDENTIFIER
anti-mouse Ly6C - BV711 (clone HK1.4)	Biolegend	Cat# 128037; RRID: AB_2562630
anti-mouse Ly6G - BV785 (clone 1A8)	Biolegend	Cat# 127645; RRID: AB_2566317
anti-mouse I-A/I-E - AF700 (clone M5/114.15.2)	Biolegend	Cat# 107622; RRID: AB_493727
anti-mouse NK1.1 - BV785 (clone PK136)	Biolegend	Cat# 108749; RRID: AB_2564304
anti-mouse PD-1 (CD279) - BV605 (clone 29F.1A12)	Biolegend	Cat# 135219; RRID: AB_11125371
anti-mouse SiglecF - BV785 (clone E50-2440)	BD BioSciences	Cat# 740956; RRID: AB_2740581
anti-mouse TCF1 - PE (clone S33-966)	BD BioSciences	Cat# 564217; RRID: AB_2687845
anti-mouse TCRb - AF488 (clone H57-597)	Biolegend	Cat# 109215; RRID: AB_493344
anti-mouse TCRb V8.1 - PE (clone MR5-2)	BD BioSciences	Cat# 553186; RRID: AB_394695
anti-mouse TNFa - BV421 (clone MP6-XT22)	Biolegend	Cat# 506327; RRID: AB_10900823
anti-mouse TNFa - PE (clone MP6-XT22)	Biolegend	Cat# 506306; RRID: AB_315427
anti-mouse TOX - APC (clone REA473)	Miltenyi Biotec	Cat# 130-118-335; RRID: AB_2751485
anti-mouse CD16/32 (clone 2.4G2)	BioXCell	BE0307
anti-mouse CD4 InVivoMab (clone GK1.5)	BioXCell	BE0003-1
anti-mouse CD8 InVivoMab (clone 2.43)	BioXCell	BE0061
anti-mouse CSF1 InVivoMab (clone 5A1)	BioXCell	BE0204
anti-mouse CSF1R InVivoMab (clone AFS98)	BioXCell	BE0213
Rat IgG1, k (clone HRPN)	BioXCell	BE0088
Rat IgG2b, k (clone LTF-2)	BioXCell	BE0090
Rat IgG2a, k (clone 2A3)	BioXCell	BE0089
Hypoxyprobe Pacific Blue kit (4.3.11.3 MAb1)	Hypoxyprobe, Inc.	hp15-100kit
Normal Rat Serum	Thermo Fisher	10710C
Biological samples		
Human tumor samples	UC San Francisco	IRB# 20-31740
Mouse tissue samples (LN, tumor)	UC San Francisco	IACUC: AN184232
Chemicals, peptides, and recombinant proteins		
Matrigel GFR	Corning	356231
Collagenase, Type I	Worthington Biochemical	LS004197
Collagenase, Type IV	Worthington Biochemical	LS004189
Dnase I	Millipore Sigma	10104159001
Ficoll-Paque Plus	GE Healthcare	17-1440-02
Ficoll-Paque Premium 1.084	GE Healthcare	17-5446-02
Zombie NIR Fixable Viability Dye	Biolegend	423106
CFSE	Invitrogen	C34554
Violet Proliferation Dye	BD Biosciences	562158
CMTMR	Thermo Fisher	C2927
Brefeldin A (BFA)	Sigma-Aldrich	B7651
Phorbol 12-myristate 12-acetate (PMA)	Sigma-Aldrich	P8139
Ionomycin	Invitrogen	I24222
Complete Freund's Adjuvant	Sigma-Aldrich	F5881
OVA peptide (257-264) SIINFEKL	Anaspec	AS-60193
LCMV gp33 peptide (33-41) KAVYNFATC	Anaspec	AS-61669
Recombinant murine IL-4	Peprotech	214-14
Recombinant murine GM-CSF	Peprotech	315-03
Recombinant human IL-2	Peprotech	200-02
Fibronectin, bovine plasma	EMD Millipore	341631
FURA-2AM	Thermo Fisher	F1221

(Continued on next page)

Continued

REAGENT or RESOURCE	SOURCE	IDENTIFIER
Critical commercial assays		
Chromium Single Cell 3' GEM Library & Gel Bead Kit V3	10x Genomics	PN-1000092
Foxp3/Transcription Factor Staining Buffer Kit	BD Biosciences	554655
EasySep Mouse CD8 ⁺ T cell Isolation Kit	STEMCELL Technologies	19853
EasySep Mouse Biotin Positive Selection Kit	STEMCELL Technologies	17665
EasySep Mouse Monocyte Isolation Kit	STEMCELL Technologies	19861
UltraComp eBeads Compensation Beads	Fisher Scientific	01-2222-42
Corning HTS Transwell 96 well permeable supports	Corning	CLS3388
RNeasy Micro kit	Qiagen	74004
High-Capacity cDNA Reverse Transcription kit	Thermo Fisher	4368814
Mouse M-CSF Quantikine ELISA kit	R&D Systems	MMC00
CBA Mouse MIP-1a Flex Set	BD BioSciences	558449
CBA Mouse MIP-1b Flex Set	BD BioSciences	558343
CBA Mouse MIP-1a Flex Set	BD BioSciences	558345
Deposited data		
All bulk RNAseq data for IPI cohort	Combes et al., (2022)	GEO:GSE184398
Bulk RNAseq and ATACseq on T cells	This paper	GEO:GSE201074
Single cell RNAseq data from CD206R ZipSeq	This paper	GEO:GSE201074
GitHub	Kenneth Hu Github	https://github.com/ken7hu/ZipSeq-Analysis-CD206R
Experimental models: Cell lines		
B16F10	AATCC	CRL-6475
B16ChOVA	UC San Francisco	N/A
B78ChOVA	UC San Francisco	N/A
Experimental models: Organisms/strains		
Mouse: C57BL/6J	The Jackson Laboratory	Stock # 000664
Mouse: B6 CD45.1 (B6.SJL-Ptprc Pepc/BoyJ)	The Jackson Laboratory	Stock # 002014
Mouse: OT-I (C57BL/6-Tg(TcraTcrb)1100Mjb/J)	The Jackson Laboratory	Stock # 003831
Mouse: mTmG	The Jackson Laboratory	Stock # 007676
Mouse: Rag1 KO (B6.129S7-Rag1tm1Mom/J)	The Jackson Laboratory	Stock # 002216
Mouse: CSF1op/op (B6;C3Fe a/a-Csf1op/J)	The Jackson Laboratory	Stock # 000231
Mouse: Csf1rCre (C57BL/6-Tg(Csf1r-cre)1Mnz/J)	The Jackson Laboratory	Stock # 029206
Mouse: LCMV P14 (crossed to B6 background)	Michael Waterfield, UC San Francisco	MGI: 2665105
Mouse: MMTV-PyMTChOVA	Matthew Krummel, UC San Francisco	MGI: 5436574
Mouse: CD206-LSL-Venus-DTR	Matthew Krummel, UC San Francisco	N/A
Oligonucleotides		
Taqman probe: Ccl3	Life Technologies	Mm00441259_g1
Taqman probe: Ccl5	Life Technologies	Mm01302427_m1
Taqman probe: Csf1	Life Technologies	Mm00432686_m1
Taqman probe: Gapdh	Life Technologies	Mm99999915_g1
Software and algorithms		
Imaris	Bitplane	https://imaris.exinst.com/
ImageJ	NIH	https://imagej.nih.gov/ij/
FlowJo	Becton Dickinson	https://flowjo.com/
CellRanger 4.0.0	10X Genomics	10xgenomics.com
Seurat	Satija et al., (2015)	https://satjalab.org/seurat
STAR	Dobin et al., (2013)	https://code.google.com/archive/p/rna-star/
R: The Project for Statistical Computing	N/A	http://r-project.org
CellChat	Jin et al., (2021)	http://www.cellchat.org/

RESOURCE AVAILABILITY

Lead contact

Further information and requests for resources and reagents should be directed to and will be fulfilled by the Lead Contact, Matthew F. Krummel (matthew.krummel@ucsf.edu).

Materials availability

All unique reagents generated in this study are available from the [lead contact](#) without restriction.

Data and code availability

Bulk RNA-seq, bulk ATAC-seq and single-cell RNA-seq data have been deposited at GEO (GEO: GSE201074) and are publicly available as of the date of publication. RNA-seq data from human tumors has been published previously ([Combes et al., 2022](#)) and is publicly available at GEO (GEO: GSE184398). Accession numbers are also listed in the [key resources table](#). All original code has been deposited to GitHub and is publicly available as of the date of publication. DOIs are listed in the [key resources table](#). Any additional information required to reanalyze the data reported in this paper is available from the [lead contact](#) upon request.

EXPERIMENTAL MODEL AND SUBJECT DETAILS

Human tumor samples

Flow cytometry on kidney renal clear cell carcinoma (KID) samples: samples were transported from various cancer operating rooms or outpatient clinics. All patients consented by the UCSF IPI clinical coordinator group for tissue collection under a UCSF IRB approved protocol (UCSF IRB# 20-31740). Samples were obtained after surgical excision with biopsies taken by Pathology Assistants to confirm the presence of tumor cells. Patients were selected without regard to prior treatment. Freshly resected samples were placed in ice-cold DPBS or Leibovitz's L-15 medium in a 50 mL conical tube and immediately transported to the laboratory for sample labeling and processing. The whole tissue underwent digestion and processing to generate a single-cell suspension. In the event that part of the tissue was sliced and preserved for imaging analysis, the remaining portion of the tissue sample was used for flow cytometry analysis as described in [Combes et al. \(2022\)](#).

Samples from the following tumor types were used for RNA-seq on FACS-isolated cell fractions performed as described previously ([Combes et al., 2022](#)): Bladder cancer (BLAD), colorectal cancer (CRC), glioblastoma multiforme (GBM), endometrial and ovarian cancer (GYN), hepatocellular carcinoma (HEP), head and neck squamous cell carcinoma (HNSC), kidney renal clear cell carcinoma (KID), lung adenocarcinoma (LUNG), skin cutaneous melanoma (MEL), pancreatic ductal adenocarcinoma (PDAC), pancreatic neuro-endocrine tumors (PNET), sarcoma (SRC).

Mice

All mice were treated in accordance with the regulatory standards of the National Institutes of Health and American Association of Laboratory Animal Care and were approved by the UCSF Institution of Animal Care and Use Committee. The following mice were purchased for acute use or maintained under specific pathogen-free conditions at the University of California, San Francisco Animal Barrier Facility: C57BL6/J, C57BL6/J CD45.1, OT-I, P14 LCMV, *Rag1^{-/-}*, *Csf1^{op/op}*, mTmG. With the exception of *Csf1^{op/op}*, all mice used in experimentation were bred to a C57BL6/J background. Mice of either sex ranging in age from 6 to 12 weeks were used for experimentation. For experiments using the transgenic *MMTV-PyMTChOVA* strain ([Engelhardt et al., 2012](#)), only mammary tumor-bearing females were used ranging in age from 12 to 20 weeks. Treatments in *MMTV-PyMTChOVA* mice were started when mammary tumors reached ~25mm² in size. *Csf1rCreCd206-LSL-Venus-DTR* mice (Ray, A. et al. *in preparation*) were generated and used for ZipSeq. Food and water were provided *ad libitum*.

Tumor cell lines

Tumor cell lines B16F10 (CRL-6475, ATCC), B16ChOVA ([Roberts et al., 2016](#); [Binnewies et al., 2019](#)) and B78ChOVA ([Engelhardt et al., 2012](#); [Broz et al., 2014](#)) were cultured under standard conditions 37°C in 5% CO₂ in DMEM (GIBCO), 10% FCS (Benchmark), 1% Pen/Strep/Glut (Invitrogen).

METHOD DETAILS

Tumor growth experiments

For tumor studies, adherent tumor cells were grown to confluence and harvested using 0.05% Trypsin-EDTA (GIBCO) and washed 3x with PBS (GIBCO). 1.0 × 105–2.5 × 105 cells in PBS were resuspended in a 1:1 ratio with Growth Factor Reduced Matrigel (Corning) and a final volume of 50µL was injected subcutaneously into the flanks of anesthetized and shaved mice. Tumors were allowed to grow for 14–21 days unless otherwise noted, before tumors and tumor-draining lymph nodes were harvested for analysis.

Adoptive T cell transfers

Inguinal, axillary, brachial and mesenteric lymph nodes (LN) or spleens were isolated from CD45.1 OT-I or P14 LCMV mice. LN and spleens were meshed through 70 μ m filters and treated with ACK red blood cell lysis buffer. CD8 $^{+}$ T cells were purified using EasySep CD8 negative selection kits (Stemcell Technologies). 1 \times 105 (for >14 days readout) – 2 \times 106 T cells (for day 4 readout) were adoptively transferred through retro-orbital injection in 100 μ L PBS.

For the comparison of OT-I T cells and p14 LCMV T cells, mice received a 1:1 mix of both T cells in 100 μ L of PBS through retro-orbital injection. The following day mice were inoculated with a bolus of CFA containing gp33-peptide (50 μ g/mouse; Anaspec) and SL8/SIINFEKL peptide (50 μ g/mouse; Anaspec) subcutaneously, to sustain both T cell populations.

In vivo antibody treatment

For macrophage depletions, mice received anti-CSF1 (clone 5A1; BioXCell), anti-CSF1R (clone AFS98; BioXCell) or corresponding isotype controls, Rat IgG1k (clone HRPN; BioXCell) and Rat IgG2a (clone 2A3; BioXCell), respectively. Antibodies were injected intra-peritoneally at an initial dose of 1mg/mouse followed by 0.5mg/mouse every 7 days.

For T cell depletion studies, mice received anti-CD4 (clone GK1.5; BioXCell), anti-CD8a (clone 2.43; BioXCell) or corresponding isotype control, Rat IgG2b (clone LTF-2; BioXCell) dosed at 250 μ g/mouse every 3–4 days.

Generation of mixed bone marrow chimeras

Mixed bone marrow chimeras were generated as described previously (Barry et al., 2018). Briefly, *Rag1* $^{-/-}$ mice were lethally irradiated with 1,100 rads of irradiation in two doses 3–5 h apart. 2–5 \times 106 bone marrow cells, consisting of 50% *Rag1* $^{-/-}$ and 50% *Csf1* $^{op/op}$ or *Csf1* $^{op/+}$ bone marrow, were injected retro-orbitally to reconstitute irradiated mice. Chimeric mice were allowed to recover for 6–10 weeks, upon which mice were inoculated with B78ChOVA tumors subcutaneously.

Mouse tissue digestion and flow cytometry

Tumors were harvested and processed to single cell suspensions as described previously (Barry et al., 2018; Binnewies et al., 2019). Briefly, tumors were isolated and mechanically minced, followed by enzymatic digestion with 200 μ g/mL DNase (Sigma-Aldrich), 100U/mL Collagenase I (Worthington Biochemical) and 500U/mL Collagenase Type IV (Worthington Biochemical) for 30 min at 37°C while shaking. Enzymatic activity was quenched by adding equal amounts of FACS buffer (2% FCS in PBS), and cell suspensions were filtered to obtain single cell suspensions. TdLN were isolated and meshed over 70 μ m filters in PBS to generate single cell suspensions. For each sample, 5–10 \times 106 cells were used for staining for flow cytometry. Cells were washed with PBS prior to staining with Zombie NIR Fixable live/dead dye (Biolegend) for 20 min at 4 °C. Cells were washed in PBS followed by surface staining for 30 min at 4°C with directly conjugated antibodies diluted in FACS buffer containing anti-CD16/32 (BioXCell) to block non-specific binding. Cells were washed again with FACS buffer. For intracellular staining, cells were fixed for 20 min at 4°C using the FOXP3 Fix/Perm kit (BD Biosciences), and washed in permeabilization buffer. Antibodies against intracellular targets were diluted in permeabilization buffer and cells were incubated for 30 min at 4°C followed by another wash prior to readout on a BD LSR Fortessa SORP cytometer.

Fluorescence activated cell sorting

Single cell suspensions from tumors were prepared as described above. For T cell isolations, single cell suspensions were enriched for mononuclear cells using Ficoll-Paque Premium 1.084 (GE Healthcare). For isolation of myeloid cells, single cell tumor suspensions were enriched for CD45 $^{+}$ cells using EasySep biotin positive selection kit (Stemcell Technologies). Enriched cells were stained for 30 min at 4°C with directly conjugated antibodies diluted in FACS buffer containing anti-CD16/32 (BioXCell) to block non-specific binding. Cells were washed again with FACS buffer and filtered over a 70 μ m mesh. Immediately prior to sorting, DAPI was added to exclude dead cells. Cells were sorted on a BD FACSAria Fusion and BD FACSAria2. Sorted T cells were collected directly in lysis buffer (Invitrogen) for RNA sequencing or in RPMI (GIBCO), 10% FCS (Benchmark), Pen/Strep/Glut (Invitrogen) and 50 μ M β -mercaptoethanol (GIBCO) at 4°C for further use ex vivo. Sorted myeloid cells were collected in DMEM (GIBCO), 10% FCS (Benchmark), Pen/Strep/Glut (Invitrogen) at 4°C for further use ex vivo.

Intracellular T cell cytokine analysis

For analysis of cytokine production by endogenous and adoptively transferred T cells, 5–10 \times 106 LN and tumor cells were re-stimulated for 3–5 h in RPMI (GIBCO), 10% FCS (Benchmark), Pen/Strep/Glut (Invitrogen), 50 μ M β -mercaptoethanol (GIBCO) containing PMA (50 ng/mL; Sigma-Aldrich), ionomycin (500 ng/mL; Invitrogen) and brefeldin A (3 μ g/mL; Sigma-Aldrich) at 37°C in 5% CO₂. Cells were washed and stained for intracellular flow cytometric analysis.

ELISA and Cytometric Bead Array

Endogenous CD8 $^{+}$ CD44 $^{-}$ (naïve) and CD8 $^{+}$ CD44 $^{+}$ (effector) T cells were isolated from lymph nodes, and CD8 $^{+}$ CD44 $^{+}$ (exhausted) T cells were isolated from tumors of B78ChOVA-bearing mice using FACS. Antigen-specific OT-I CD8 $^{+}$ CD44 $^{-}$ (naïve) T cells were isolated directly from lymph nodes of tumor-free OT-I transgenic mice, or activated *in vitro* with antigen-pulsed splenocytes to generate effector OT-I T cells. Congenically labeled (CD45.1) OT-I CD8 $^{+}$ CD44 $^{+}$ T cells were isolated from B78ChOVA tumors >14 days after adoptive transfer (exhausted T cells). Isolated T cells (3 \times 105) were cultured *ex vivo* in RPMI (GIBCO),

10% FCS (Benchmark), Pen/Strep/Glut (Invitrogen), 50 μ M β -mercaptoethanol (GIBCO) for 24 h. Levels of secreted CSF1 in supernatant was measured by ELISA (R&D Systems). Levels of secreted CCL3, CCL4 and CCL5 in supernatant were measured by Cytometric Bead Array (CBA) CCL3/MIP-1 α , CCL4/MIP-1 β and CCL5/RANTES Flex Sets (BD BioSciences) according to manufacturer's recommendations.

RNA sequencing

mRNA from cells were isolated using DynaBead Direct and then converted into amplified cDNA using the Tecan Ovation RNA-Seq System V2 kit, following the manufacturer guidelines. The dsDNA is fragmented, amplified and undergoes clean up with AMPure XP bead, using the Illumina Nextera XT DNA Library Prep Kit. The resulting sequencing library is QC'd using an Agilent Bioanalyzer HS DNA chip to assess fragment size distribution and concentration. Libraries were pooled prior to single-end sequencing on an Illumina MiSeq/MiniSeq to ensure quantify library complexity. Libraries with less than 10 percent of the reads aligned to coding regions, or fewer than 1,000 unique reads in total were rejected. The validated libraries were re-pooled based on the percentage of reads in coding regions and submitted to the UCSF Center for Advanced Technology for 150bp paired end sequencing on an Illumina NovaSeq 6000.

Raw fastq reads were QC'd and trimmed to remove adapter contamination, and poly-G artifacts using fastp version 0.19.6 ([Chen et al., 2018](#)). Reads with fewer than 20bp post-trimming were discarded. Trimmed reads were aligned to the GRCh38 reference sequence annotated with Gencode V25 ([Frankish et al., 2019](#)) using STAR version 2.6.1b ([Dobin et al., 2013](#)) with the following parameters (`--quantMode GeneCounts --outFilterMismatchNoverLmax 0.04 --alignIntronMax 100000 --alignMatesGapMax 100000 --alignSJDBoverhangMin 10 --alignSJstitchMismatchNmax 5 -1 5 5 --chimSegmentMin 12 --chimJunctionOverhangMin 12 --chimSegmentReadGapMax 3 --chimMultimapScoreRange 10 --chimMultimapNmax 10 --chimNonchimScoreDropMin 10 --peOverlapNbasesMin 12 --peOverlapMMp 0.1`). STAR-generated reads counts from each library were processed using the limma/Voom pipeline ([Law et al., 2014](#); [Smyth, 2005](#)) using the edgeR package ([Robinson et al., 2010](#)). Briefly, the read counts are loaded into a DGEList object to generate Counts Per Million (CPM), and then filtered to retain only genes with at least 10 counts in a worthwhile number of samples and at least 15 counts across all samples. The CPM matrix is normalized using TMM Trimmed mean of M-values and processed using voom to estimate the mean-variance relationship to identify edge weights that can be used to fit to a linear model with limma lmFit. Differential gene expression between two groups of empirical Bayes moderation of the standard errors toward a global value. A list of transcriptional DE-Gs between Tnaive and Tex d14 with an FC equal to or >5 was generated and gene set enrichment analysis was performed using the MGI Mammalian Phenotype Level 4 database in Enrichr ([Chen et al., 2013](#); [Kuleshov et al., 2016](#); [Xie et al., 2021](#)).

ATAC sequencing

ATAC-seq samples were processed according to the Omni-ATAC protocol ([Corces et al., 2017](#)). 5 \times 104 cells per replicate were lysed in 50 μ L ATAC resuspension buffer supplemented with 0.1% NP40, 0.1% Tween 20, and 0.01% Digitonin. After lysis, nuclei were transposed using 2.5 μ L Tn5 transposase in a 50 μ L reaction for 30 min at 37°C. Finally, the transposed DNA was purified using a commercial PCR cleanup kit and libraries were prepared for sequencing. 2 \times 75 paired end sequencing was performed on an Illumina sequencer.

ATAC-seq computational analysis was performed as previously described ([Weber et al., 2021](#)). Briefly, read trimming and filtering was performed with fastp. Reads were mapped to the hg38 reference genome using hisat2 with the `--no-spliced-alignment` option. Picard was used to remove duplicates from bam files. We removed any reads not mapping to chromosomes 1–22 and chrX (ie chrY reads, mitochondrial reads, and other reads were discarded). The deduplicated and filtered fragments were then formatted into a bed file. Peaks were called using MACS2. Peaks from each sample were iteratively merged into a high confidence union peak set for all samples as previously described ([Corces et al., 2018](#)). A peak by sample matrix was created by overlapping fragments in each sample with each peak, and this matrix was used to perform differential peak analysis in DESeq2. Genome coverage files were created from the fragments file by loading the fragments into R and then exporting bigwig files normalized by reads in transcription start sites using ‘rtracklayer::export’. Normalized track files were visualized using the Integrative Genomics Viewer.

qRT-PCR

RNA was extracted from FACS-sorted immune cell populations using Qiagen RNeasy Micro kit (Qiagen) and the yield was measured using Nanodrop. cDNA first-strand synthesis was performed using High-Capacity cDNA Reverse Transcription kit (Thermo Fisher Scientific) using random primers. qRT-PCR analysis was performed using Taqman probes targeting Ccl3 (Mm00441259_g1), Ccl5 (Mm01302427_m1), Csf1 (Mm00432686_m1) and Gapdh (Mm99999915_g1). All probes were obtained from Life Technologies. For amplification reactions, iTaq Universal Probes Supermix was used according to manufacturer's instructions. qRT-PCR was performed on a QuantStudio 12K Flex lightcycler (Applied Biosystems by Life Technologies). For quantification the delta Ct method was used: delta Ct sample — delta Ct reference gene. All transcripts were normalized to Gapdh.

Monocyte recruitment transwell assays

Bone marrow was obtained from femurs and tibia of CD45.1 mice, and monocytes were isolated using EasySep Mouse Monocyte Isolation kits (Stemcell Technologies). For transwell assays, 1 \times 105 monocytes were added to top inserts containing 5.0 μ m pore

polycarbonate membrane (Corning). 0.5×10^5 naïve, previously activated or exhausted OT-I T cells were cultured in bottom wells in RPMI (GIBCO), 10% FCS (Benchmark), Pen/Strep/Glut (Invitrogen) and 50 μ M β -mercaptoethanol (GIBCO). Migration through the membrane was analyzed after 24 h of culture. Plate was briefly centrifuged briefly at 1000rpm for 1 min to collect cells stuck to the membrane. Cells were collected for analysis by flow cytometry. Absolute counting beads (Life Technologies) were added for quantification of the number of migrated cells.

Generation of activated T cells

OT-I T cells were activated *in vitro* as described previously (Broz et al., 2014). Briefly, OT-I lymph node cells were stimulated with B6 splenocytes pulsed with SL8 peptide (100 ng/mL; Anaspec) for 30 min at 37°C and then washed 3 times. On day 2–3, cells were expanded by adding human IL-2 (2U/mL; Peprotech) to fresh RPMI (GIBCO), 10% FCS (Benchmark), Pen/Strep/Glut (Invitrogen), 50 μ M β -mercaptoethanol (GIBCO). Cells were used for co-culture assays on day 4–5. Prior to use dead cells were excluded using Ficoll-Paque PLUS (GE Healthcare).

Bone marrow-derived dendritic cells

BMDC were generated as described previously (Broz et al., 2014). Briefly, bone marrow was obtained from femurs and tibia of C57BL6/J mice and cultured in DMEM (GIBCO), 10% FCS (Benchmark), Pen/Strep/Glut (Invitrogen) in the presence of 7.5 ng/mL GM-CSF (Peprotech) for 6–8 days, followed by the addition of 60 ng/mL IL4 (Peprotech) for the last 2 days. Media was refreshed every 3–4 days. For co-cultures studies, BMDC were pulsed with SL8 peptide (100 ng/mL; Anaspec) for 30 min at 37°C and then washed 3 times prior to use.

Quantification of APC-T cell interactions

APC (BMDC, BMDC+SL8 or sorted TAM) were obtained from mTmG mice, and previously activated OT-I T cells were stained for 15 min at 37°C with 2 μ M CFSE (Invitrogen) in PBS and washed in RMPI prior to use. Cells were co-cultured in NUNC 8 well chamber slides (Thermo Scientific) that were coated with fibronectin (2 μ g/mL; EMD Millipore) in PBS at 37°C for 1 h before use. APCs in phenol red-free RPMI were allowed to attach to the chamber slides for 20–30 min at 37°C and 5% CO₂. Right before imaging, T cells (re-suspended in 0.1% agarose) were added to the wells and slides were loaded for imaging. To visualize the interaction between different APC populations and T cells, a conventional widefield Zeiss Axiovert 200M was used with a Sutter Lambda XL illumination source, running on μ Magellan software. Images were acquired every 2 min for 6 h using a 20x objective. Samples were kept at 37°C using a heated robotic stage. Image analysis was performed in Imaris (Bitplane) and ImageJ.

APC-T cell coupling assay

Ex vivo coupling assays were performed as described previously (Broz et al., 2014). Briefly, single cells suspensions were enriched for CD45⁺ cells using EasySep biotin positive selection kit (Stemcell Technologies). Enriched cells were stained with with Zombie NIR Fixable live/dead dye (Biolegend) for 20 min at 4°C, followed by staining for 30 min at 4°C with directly conjugated antibodies diluted in FACS buffer containing anti-CD16/32 (BioXCell) to block non-specific binding. Cells were washed again and co-cultured with VPD-labeled previously activated OT-I CD8⁺ T cells for 1 h at 37°C. Cells were lightly fixed in 2% PFA followed by readout on a BD LSR Fortessa SORP cytometer.

Lattice light-sheet imaging

Lattice light-sheet (LLS) imaging was performed in a manner previously described (Cai et al., 2017). Briefly, 5 mm diameter round coverslips were cleaned by a plasma cleaner and coated with fibronectin (2 μ g/mL; EMD Millipore) in PBS at 37°C for 1 h before use. TAM sorted from B78ChOVA-bearing mTmG mice were dropped onto the coverslip and incubated at 37°C, 5% CO₂ for 20–30 min. Previously activated OT-I CD8⁺ T cells were labeled with CD45-AF647 (clone 30-F11; Biolegend) and TCR β AF488 (clone H57-597; BioLegend) for 30 min and washed in FACS buffer. Right before imaging, T cells were dropped onto the coverslip containing TAM. The sample was then loaded into the previously conditioned sample bath and secured. Imaging was performed with a 488-nm, 560-nm, or 642-nm laser (MPBC, Canada) dependent upon sample labeling in single or two-color mode. Exposure time was 10 ms per frame leading to a temporal resolution of 4.5 s. Image renderings were created using Imaris software (Bitplane). Quantification of TCR clustering was performed using ImageJ. Briefly, channels were separated and entire T cell membrane versus TAM interaction site was outlined manually. Signal intensity for red (CD45) and green (TCR) channel was calculated. The following formula was used to determine TCR signal intensity for both channels at the synaptic TAM-T cell interaction site: signaling intensity = (intensity at synapse/intensity total membrane).

FURA-2AM calcium imaging

TAM or CD103 + DC were sorted from B16ChOVA or B16F10 tumors as per description above, and stained with 2 μ M CMTMR (Thermo Fisher Scientific) in PBS for 15 min at 37°C, followed by a wash in RPMI. Cells were co-cultured in NUNC 8 well chamber slides (Thermo Scientific) that were coated with fibronectin (2 μ g/mL; EMD Millipore) in PBS at 37°C for 1 h before use. APCs in phenol red-free RPMI were allowed to attach to the chamber slides for 20–30 min at 37°C and 5% CO₂. Right before imaging, previously activated OT-I T cells were labeled with FURA-2 AM (0.5 μ M; Invitrogen) for 15 min at RT. Cells were washed and resuspended in phenol red-free RPMI (GIBCO), 10% FCS (Benchmark), Pen/Strep/Glut (Invitrogen), 50 μ M β -mercaptoethanol (GIBCO)

supplemented with 0.1% agarose and were added to the wells. Imaging was performed using an Zeiss Axiovert 200M microscope with a Sutter Lambda XL illumination source equipped with a 40x oil objective. Images were acquired every 5 s for 18–21 min. Samples were kept at 37°C using a heated robotic stage. Image analysis was performed in Imaris (Bitplane). Briefly, background subtraction was performed and surfaces were created for APCs and T cells to quantify dwell time to determine whether cells were touching (cut-off equal to or >3). Calcium²⁺ flux was determined by calculating the average 340/380 ratiometric fluorescence per cell after contact for each time point.

Hypoxyprobe imaging

Mice were injected with pimonidazole hydrochloride in PBS (80 mg/kg; Hypoxyprobe) intraperitoneally 1.5 h prior to sacrifice. Tissues were dissected and processed as described above. For flow cytometry studies, pimonidazole was visualized using anti-pimonidazole antibodies (Pacific Blue Mab-1 clone 4.3.11.3; Hypoxyprobe) after cells were fixed for 20 min at 4°C using the FOXP3 Fix/Perm kit (BD Biosciences), and washed in permeabilization buffer. For imaging studies, dissected tumors were embedded in OCT and sectioned into 10 µm cryosections. Cryosections were stored at -80°C until further use. For immunostaining, sections were fixed in 4% PFA (Electron Microscopy Sciences) for 20 min at RT, followed by a rinse in PBS containing 1% BSA (Sigma). Sections were blocked in 1% BSA in PBS containing anti-CD16/32 (BioXCell) for 1 h at RT, and washed. Sections were stained with CD11b-AF594 (clone M1/70; BioLegend), CD31-AF647 (clone 390; BioLegend) and Pacific Blue Mab-1 (clone 4.3.11.3; Hypoxyprobe) for 1 h at RT, followed by a wash and mounted using Vectashield (Vector Laboratories) and sealed with nail polish. Images were acquired on a Leica SP8 confocal microscope. Data analysis was performed using Imaris (Bitplane).

In vitro APC-T cell co-culture assays

APC populations were sorted from tumors as described above, and co-cultured with 1 × 10⁵ previously activated OT-I CD8⁺ T cells labeled with Violet Proliferation dye (VPD; BD Biosciences) at a 1:5 ratio (unless otherwise noted) in RPMI (GIBCO), 10% FCS (Benchmark), Pen/Strep/Glut (Invitrogen), 50 µM β-mercaptoethanol (GIBCO) in 96-well round bottom plates. Cells were harvested for analysis 3 days later, unless otherwise noted. *In vitro* generated BMDC and BMDC + SL8 were used as negative and positive controls, respectively.

For hypoxia experiments, plates containing exact same experimental groups were incubated in an Avatar hypoxic bioreactor (XcellBio) at 1.5% O₂ or under ambient 21% O₂ for comparison and cells were harvested after 3 days.

ZipSeq

ZipSeq spatial transcriptomics was performed as described previously (Hu et al., 2020). Briefly, B78ChOVA cells were injected subcutaneously as described above and were harvested day 16 post-injection. Tumors were sectioned while live using a compressstome (Precisionary Instruments VFZ-310-0Z) to generate ~160 µm sections. The sectioning, imaging, spatial barcoding, tumor dissociation, sorting, 10X encapsulation and library construction were identical to the methods described in (Hu et al., 2020). The targeted number of cells for loading was 5000. With this in mind, we aimed for 30,000 reads per cell during sequencing on an Illumina S4 flow-cell with a 1:10 molar ratio of Zipcode reads to gene expression reads. Resulting fastq files were processed using the CellRanger 4.0.0 pipeline, aligning to the GRCm38 *Mus musculus* assembly. CellRanger output thus resulted in ~359k reads for the gene expression library and ~40k reads for the Zipcode library.

Analysis of scRNA-Seq

The raw feature-barcode matrix generated by 10X CellRanger was loaded into Seurat (Satija et al., 2015). Cells with mitochondrial read % over 20% and those with less than 500 genes detected were excluded from analysis. Zipcode read counts from CellRanger were also loaded into Seurat as a separate 'ADT' assay and using CLR normalized counts, cells with either too few Zipcode reads or mixed Zipcode reads were also excluded from analysis. Following built-in Seurat methods for gene expression normalization and variance stabilization (Single Cell Trans-form (Hafemeister and Satija, 2019)), cells underwent one more round of clean-up, removing a small cluster of contaminating CD45- cells and another small cluster dominated by mitochondrial and ribosomal genes. This yielded 2765 cells. At this stage, the mean # of UMI's and # of detected genes was: (25,566 and 4,199 respectively) while for the antibody derived Zipcode tags the mean UMI was 1,891 reads. At this stage, we also determined cluster identities using Seurat's FindAllMarkers function performed on the log-normalized read counts which by default uses the Wilcoxon Rank Sum test.

For CellChat analysis, this cleaned object was fed into the CellChat workflow, using the built-in mouse ligand-receptor database, and a tri-mean thresholding for significance of interaction. The Seurat object was split into 3 sub-objects based on regional assignment and these 3 objects were separately analyzed using the CellChat workflow for multiple datasets and then merged. For signature score generation, we used Seurat's built-in AddModuleScore function with gene lists for Glycolysis (Argüello et al., 2020), T cell exhaustion (Wherry et al., 2007), and Antigen Presentation (GO term 0048002) using 50 control features. Full gene lists can be found in Table S1. For pseudotime analysis, the monocyte/macrophage sub-object was passed into Monocle v3 without any changes to the UMAP dimensional reduction.

QUANTIFICATION AND STATISTICAL ANALYSIS

Statistical analysis

Unless specifically noted, all data are representative of ≥ 2 separate experiments. Experimental group assignment was determined by random designation. Statistical analyses were performed using GraphPad Prism software. Error bars represent \pm SE of the mean (SEM) calculated using Prism. Specific statistical tests used were paired t-tests, unpaired t-tests, and one-way ANOVA unless otherwise noted. *P*-values <0.05 were considered statistically significant. Investigators were not blinded to group assignment during experimental procedures or analysis.